

# Localized Triggering of the Insulator-Metal Transition in VO<sub>2</sub> Using a Single Carbon Nanotube

Stephanie M. Bohachuk,<sup>†</sup> Miguel Muñoz Rojo,<sup>‡,§</sup> Gregory Pitner,<sup>†</sup> Connor J. McClellan,<sup>†</sup> Feifei Lian,<sup>†</sup> Jason Li,<sup>§</sup> Jaewoo Jeong,<sup>||</sup> Mahesh G. Samant,<sup>||</sup> Stuart S. P. Parkin,<sup>||</sup> H.-S. Philip Wong,<sup>†</sup> and Eric Pop<sup>\*,†,⊥</sup>

<sup>†</sup>Department of Electrical Engineering, Stanford University, Stanford, California 94305, United States

<sup>‡</sup>Department of Thermal and Fluid Engineering, University of Twente, 7500 AE Enschede, The Netherlands

<sup>§</sup>Asylum Research, Santa Barbara, California 93117, United States

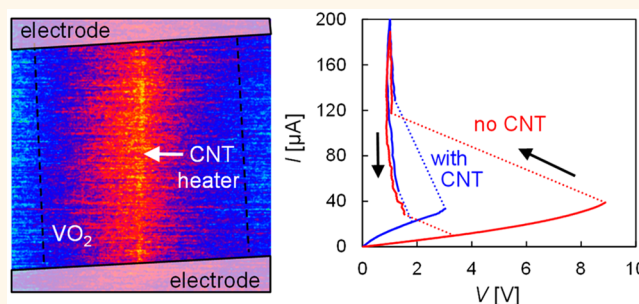
<sup>||</sup>IBM Almaden Research Center, San Jose, California 95120, United States

<sup>⊥</sup>Department of Materials Science and Engineering, Stanford University, Stanford, California 94305, United States

## Supporting Information

**ABSTRACT:** Vanadium dioxide (VO<sub>2</sub>) has been widely studied for its rich physics and potential applications, undergoing a prominent insulator-metal transition (IMT) near room temperature. The transition mechanism remains highly debated, and little is known about the IMT at nanoscale dimensions. To shed light on this problem, here we use ~1 nm-wide carbon nanotube (CNT) heaters to trigger the IMT in VO<sub>2</sub>. Single metallic CNTs switch the adjacent VO<sub>2</sub> at less than half the voltage and power required by control devices without a CNT, with switching power as low as ~85 μW at 300 nm device lengths. We also obtain potential and temperature maps of devices during operation using Kelvin probe microscopy and scanning thermal microscopy. Comparing these with three-dimensional electrothermal simulations, we find that the local heating of the VO<sub>2</sub> by the CNT plays a key role in the IMT. These results demonstrate the ability to trigger IMT in VO<sub>2</sub> using nanoscale heaters and highlight the significance of thermal engineering to improve device behavior.

**KEYWORDS:** vanadium dioxide, insulator-metal transition, carbon nanotube, scanning probe microscopy



Materials with an abrupt insulator-metal transition (IMT) have garnered much interest, both to study the role of electron correlations in creating new electronic phases and for their variety of potential applications in optics and electronics.<sup>1,2</sup> Vanadium dioxide (VO<sub>2</sub>) has one of the most pronounced transitions among these, with a structural transition from monoclinic to rutile at ~340 K. This results in a drop of electrical resistivity by up to 5 orders of magnitude, accompanied by significant changes in optical properties.<sup>3,4</sup> This transition can be induced electrically on a subnanosecond time scale by using current flow, and reverses once the stimulus is removed.<sup>5</sup> These properties have made VO<sub>2</sub> a candidate for threshold switches and selectors,<sup>6–8</sup> transistors,<sup>9,10</sup> oscillators,<sup>11,12</sup> and tunable metamaterials for optoelectronics.<sup>13–16</sup>

Integrating IMT materials with modern semiconductor technology to build these applications will require knowledge of their behavior at nanoscale dimensions. For example,

electrical devices based on two-terminal switching of VO<sub>2</sub> are expected to offer faster,<sup>5</sup> lower voltage,<sup>17–19</sup> and lower energy<sup>2</sup> switching as they are reduced to smaller dimensions, similar to devices based on phase-change materials like Ge<sub>2</sub>Sb<sub>2</sub>Te<sub>5</sub>.<sup>20,21</sup> Most two-terminal VO<sub>2</sub> devices studied to date have had dimensions ranging from ~20 nm to a few microns,<sup>19</sup> with IMT behavior preserved in all cases. It remains to be seen if the IMT in electrical devices changes once even smaller dimensions are reached. Moreover, the nanoscale triggering mechanism of VO<sub>2</sub> is not completely understood, with some debate on the role of Joule heating<sup>22</sup> vs electric field effects and carrier injection.<sup>23,24</sup> The distinction partly arises from the origin of the IMT (e.g., a Peierls structural transition triggered by heating and electron-phonon coupling vs a Mott electronic

**Received:** May 2, 2019

**Accepted:** August 8, 2019

**Published:** August 8, 2019

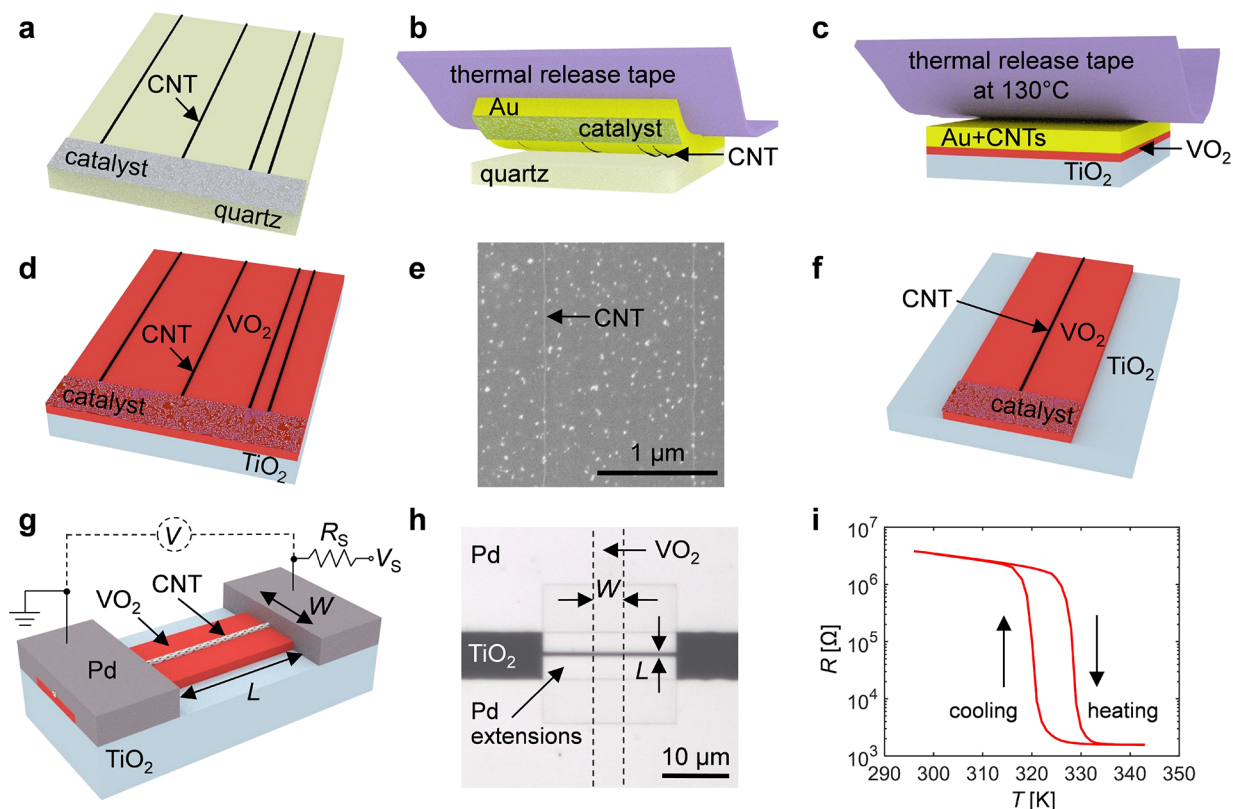


**Figure 1.** Fabrication process (layers are not to scale). (a) Aligned CNTs are grown on ST-cut quartz *via* CVD, with Fe catalyst particles.<sup>27</sup> (b) Au is e-beam evaporated onto the CNTs, then peeled off the quartz using thermal release tape. (c) The Au-coated CNTs are pressed onto VO<sub>2</sub> grown epitaxially by pulsed laser deposition (PLD) on TiO<sub>2</sub>.<sup>28</sup> The thermal release tape is then removed by heating to 130 °C. (d) After a plasma clean to remove remaining tape adhesive, the Au is wet-etched, leaving behind CNTs on VO<sub>2</sub>. (e) SEM image of CNTs on VO<sub>2</sub>. The small dots are residue left by the transfer process. (f) Excess CNTs outside planned VO<sub>2</sub> stripes are removed with an O<sub>2</sub> plasma, then the VO<sub>2</sub> is wet etched in diluted nitric acid. (g) Schematic of a fabricated VO<sub>2</sub> device with CNT heater and measurement setup, after e-beam evaporation and lift-off of Pd contacts. The width, *W*, and length, *L*, of the patterned VO<sub>2</sub> region are as labeled. The thickness of the VO<sub>2</sub> is ~5 nm in finished devices after all processing steps. Similar control devices were fabricated without CNT heaters. (h) For shorter devices, additional Pd contact extensions are added. Optical image of a short (*L* = 520 nm, *W* = 3.9 μm) VO<sub>2</sub> device. (i) Measured resistance of a VO<sub>2</sub> device without a CNT heater as a function of stage temperature. (*L* = 5 μm, *W* = 7 μm).

transition based on carrier concentration) and will provide insight into the types of devices that can be designed.

In this work, we probe the mechanism of VO<sub>2</sub> switching at the nanoscale. To extend below the limits of lithography, we use single-wall metallic carbon nanotube (CNT) heaters to trigger the VO<sub>2</sub> transition. Due to their ~1 nm diameter, such metallic CNTs are ideal candidates for probing a nanoscale phase change or IMT, as Joule heaters (capable of reaching ~600 °C in air and ~2000 °C in vacuum) or electrodes.<sup>25,26</sup> By using the localized heating of a metallic CNT, we are able to initiate the IMT at the nanoscale, at a lower power than relying on Joule heating in the VO<sub>2</sub> itself, which is promising for the development of applications requiring nanoscale VO<sub>2</sub> devices. We also use Kelvin probe microscopy (KPM) and scanning thermal microscopy (SThM) to obtain high-resolution spatial maps of the electric potential and temperature changes in our devices during operation, to understand their switching mechanism. We find good agreement between our experimental results and electrothermal simulations, confirming that Joule heating plays a major role in our devices, both with and without a CNT.

## RESULTS AND DISCUSSION

We fabricated nearly 1000 two-terminal VO<sub>2</sub> devices with and without CNTs on top. Aligned CNT arrays were grown on a separate quartz substrate, then transferred<sup>27</sup> onto thin films of single crystal VO<sub>2</sub> grown epitaxially<sup>28</sup> on TiO<sub>2</sub> (101), as illustrated in Figure 1a–d. The CNTs were coated with 100 nm of Au by electron-beam (e-beam) evaporation, then peeled off the quartz and transferred onto VO<sub>2</sub> using thermal release tape. The Au was wet-etched to leave only CNTs on VO<sub>2</sub> (see Methods for additional details). A scanning electron microscope (SEM) image of transferred CNTs on VO<sub>2</sub> is shown in Figure 1e. Excess CNTs were removed, and the VO<sub>2</sub> was wet etched into stripes (Figure 1f, also see Methods). E-beam evaporated Pd contacts were added to make complete devices, as shown in Figure 1g,h.

We used electrical testing and atomic force microscopy (AFM) scans to select devices with single metallic CNTs for further study and for comparison to control devices without a CNT. (The selection process and comparisons with multiple CNT or with semiconducting CNT devices are described in the Supporting Information Section 2.) Figure 1g shows the schematic of a VO<sub>2</sub> device with a single CNT heater, both extending underneath Pd contacts. A series resistor *R<sub>S</sub>* is used as a current compliance to protect devices from overheating

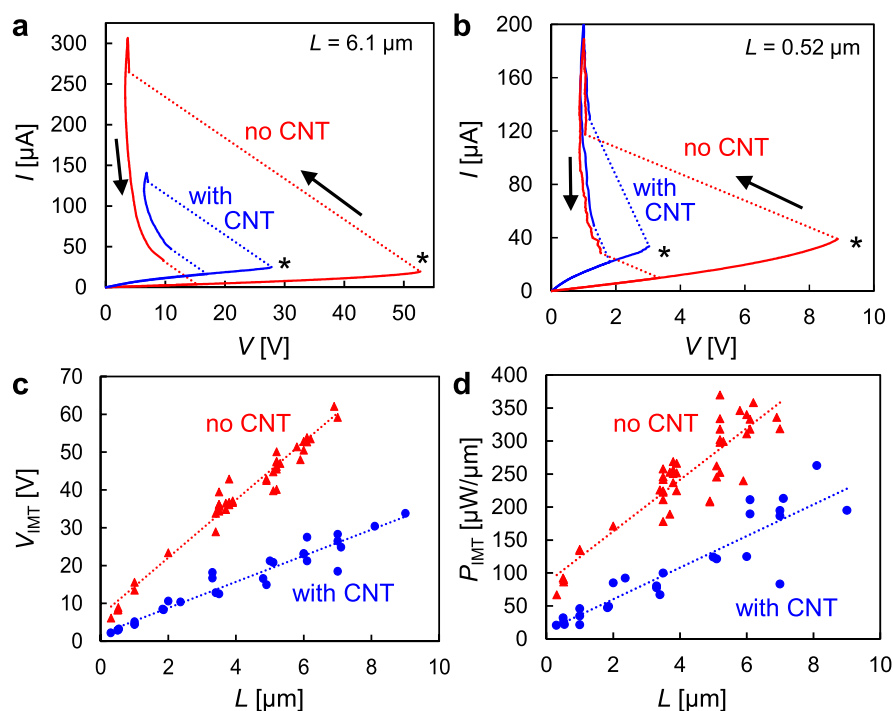


**Figure 2.** Electrical switching of devices with and without a CNT. (a) Typical switching of “long” devices with and without a CNT ( $L = 6.1 \mu\text{m}$ ,  $W = 3.2 \mu\text{m}$ ) using DC voltage control. (b) Typical switching of “short” devices with and without a CNT ( $L = 520 \text{ nm}$ ,  $W = 4 \mu\text{m}$ ) using DC voltage control. The short devices and the devices with a CNT heater have much lower switching voltages,  $V_{\text{MIT}}$ , labeled with \* on the figures. Arrows show voltage sweep directions, and dashed lines indicate snapbacks. (c) Measured  $V_{\text{MIT}}$  as a function of length for devices with (blue circles) and without (red triangles) a CNT. Dotted lines represent a linear fit. (d) Switching power,  $P_{\text{MIT}}$ , normalized by VO<sub>2</sub> width, for devices with (blue circles) and without (red triangles) a CNT. The dotted lines represent a linear fit. Adding a CNT approximately halves switching power at all length scales.

failure in the metallic state and to reduce current overshoot from external capacitance (e.g., cables and probe arm). The  $R_S$  value (20–200 kΩ) is chosen to be a small fraction of the insulating VO<sub>2</sub> resistance, but higher than the metallic VO<sub>2</sub> resistance, as detailed in the Supporting Information Section 2. Figure 1h shows an optical image of a shorter device, fabricated by adding Pd contact extensions. The measured resistance of a VO<sub>2</sub> device without a CNT is shown in Figure 1i as a function of stage temperature, displaying the transitions at  $\sim 328$  and  $\sim 321$  K for heating ( $T_{\text{MIT}}$ ) and cooling ( $T_{\text{MIT}}$ ), respectively, and a change in resistance over three orders of magnitude.

Figure 2a compares typical measured voltage-controlled  $I$ – $V$  characteristics of VO<sub>2</sub> devices with and without a CNT ( $L = 6 \mu\text{m}$ ) at room temperature ( $T_0 = 296$  K). Electrical switching is repeatable and independent of bias polarity, with similar behavior consistently observed across hundreds of devices. The non-CNT device behaves linearly as a resistor, until significant Joule heating begins to occur. As the VO<sub>2</sub> temperature increases, it becomes more conductive, and the  $I$ – $V$  curve is increasingly superlinear. Once the transition occurs at a critical voltage  $V_{\text{MIT}}$ , most of the applied bias is dropped across  $R_S$ , causing a snapback in device voltage. In the metallic state,  $R_S$  dominates over the VO<sub>2</sub> resistance, limiting the maximum current, power, and on/off ratio observed. Because  $R_S$  is used to limit heating, if devices were operated at much shorter time scales, then  $R_S$  could likely be reduced, recovering more of the intrinsic on/off ratio of the VO<sub>2</sub>.  $R_S$  can also be used to control the resistance and volume of the VO<sub>2</sub> that is metallic (Supporting Information Figure S8).

There are significant differences in the  $I$ – $V$  characteristics when a single metallic CNT is present. Prior to the IMT there is higher current and a sublinear behavior typical of current saturation due to self-heating in the CNT.<sup>29</sup> The IMT of the VO<sub>2</sub> occurs at much lower power, because the (hot) CNT is able to switch a highly localized VO<sub>2</sub> region at significantly lower voltage compared to Joule heating within the entire VO<sub>2</sub>. Once an initial region of VO<sub>2</sub> below the CNT has switched, the increased current from the metallic VO<sub>2</sub> becomes self-sustaining, and the metallic region can expand, leading to a large and abrupt increase in current. The metal-insulator transition (MIT) that occurs when the voltage is ramped back down is unaffected by the CNT, which no longer carries the majority of the current once the voltage snapback occurs. Hysteresis is observed in both types of devices because  $T_{\text{MIT}} \neq T_{\text{MIT}}$  and because at a given voltage, metallic VO<sub>2</sub> will cause more heating ( $\propto V^2/R$ ) than insulating VO<sub>2</sub>. Due to the reduction in  $V_{\text{MIT}}$ , devices with a CNT have a significantly smaller total hysteresis window. As expected, both types of devices show a decrease in  $V_{\text{MIT}}$  with rising ambient temperature (Supporting Information Section 2). At all temperatures measured, devices with a CNT display lower switching voltage and power compared to control devices without a CNT.

These differences in  $I$ – $V$  characteristics of VO<sub>2</sub> devices with and without a CNT are also seen at shorter length scales (i.e., Pd contact separation), shown in Figure 2b. Switching is consistently triggered by the  $\sim 1$  nm-wide CNT at all length scales, shown in Figure 2c–d. The presence of a CNT halves the required switching voltage and power in all devices

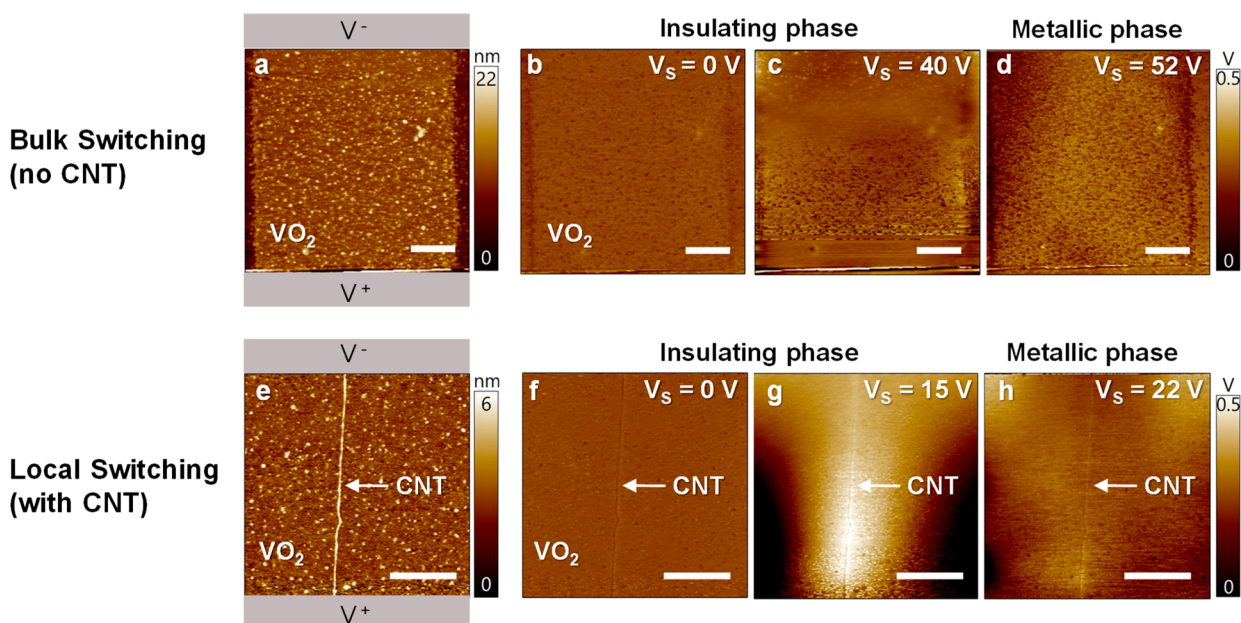


**Figure 3.** Topography and Kelvin probe microscopy (KPM) of VO<sub>2</sub> devices with and without a CNT. (a) Topography of VO<sub>2</sub> control device without a CNT. (b–d) Flattened KPM images of the same device with increasing bias  $V_s$  (also see Figure 1g). The Pd electrodes are outside the top and bottom margins of the device images, biased as marked. (e) Topography of a VO<sub>2</sub> device with a single metallic CNT, indicated by the arrow. (f–h) Flattened KPM images of the same device with increasing bias, revealing localized switching caused by the CNT. All scale bars are 1  $\mu\text{m}$ .

measured, including our shortest 300 nm lengths. Figure 2c shows that switching voltage scales linearly with length for both devices types. (Width scaling of our VO<sub>2</sub> devices is displayed in Supporting Information Figures S4 and S15.) Shorter devices have lower resistance and higher Joule heating at a given voltage, thus requiring a lower voltage and power for switching. An effective switching field can be extracted from the slope of the linear fits in Figure 2c, giving  $3.5 \pm 0.2 \text{ V}/\mu\text{m}$  with a CNT and  $7.6 \pm 0.2 \text{ V}/\mu\text{m}$  without, though this does not necessarily indicate a field-switching mechanism. If switching were triggered by field effects such as carrier injection, then the field extracted would be a description of the VO<sub>2</sub> quality and the efficiency of the switching mechanism. For a Joule heating mechanism, the field would be determined by the electrical and thermal properties of the materials that set the maximum device temperature (including ambient temperature, uniformity of heating, thermal conductivities and thermal boundary resistances, resistivities, etc.).

The vertical axis intercept in Figure 2c ( $2.0 \pm 0.8 \text{ V}$  with a CNT and  $6.8 \pm 1.0 \text{ V}$  without) corresponds to the voltage drop (contact resistance) and heat loss at the contacts.<sup>19</sup> This intercept depends on the contact material<sup>17</sup> and its temperature-dependent contact resistivity.<sup>30,31</sup> The large difference between the intercept of devices with and without a CNT is likely due to a lower contact resistance of Pd to the CNT than the VO<sub>2</sub>. An estimate of the contact resistance at switching can be found using the intercept and typical switching currents (Supporting Information Figure S3), giving  $32 \pm 15 \text{ k}\Omega$  and  $123 \pm 48 \text{ k}\Omega$  for devices with and without a CNT, respectively. This is consistent with other estimates (Supporting Information Section 2),<sup>29,32</sup> but due to non-uniform current flow, a full interpretation of these values is difficult. The ratio between the voltage drop at the contacts and the effective switching field yields a characteristic length below which the switching voltage could be contact-dominated,  $\sim 0.6 \mu\text{m}$  and  $\sim 0.9 \mu\text{m}$  in our

devices with and without a CNT, respectively. Although the power reduction observed in devices with a CNT comes partly from localized switching reducing the required field, a significant part comes from the difference in contact resistance, which could limit the switching voltage and temperature in nanoscale thin-film devices.

Given that the switching current is similar between devices with and without CNTs for the device dimensions used (Supporting Information Figure S3), Figure 2d shows that there is a reduction in power at all length scales by using a CNT. Normalization by VO<sub>2</sub> width is appropriate for devices without a CNT, but adds spread in the  $P_{\text{IMT}}$  of devices with a CNT, whose switching does not depend on the VO<sub>2</sub> width. Power scales linearly with device length, and our shortest devices with and without a CNT have switching powers of 85  $\mu\text{W}$  and 260  $\mu\text{W}$ , respectively, among the lowest reported at similar  $\Delta T = T_{\text{IMT}} - T_0$ .<sup>6,19</sup> It is expected that further reducing our device length and width would reduce switching power. These results demonstrate the feasibility of VO<sub>2</sub> switching down to the nanoscale, with its IMT behavior preserved, and that there are power benefits to doing so.

The debate regarding thermal and non-thermal IMT effects prompts us to examine whether our electrical results can be explained solely by Joule heating. To gain insight into the switching mechanism of devices with a CNT, we utilize KPM and SThM scanning probe techniques. KPM is a non-contact scanning probe technique that detects changes in the surface potential across a sample.<sup>33</sup> We use KPM to study the potential in biased VO<sub>2</sub> devices with and without a CNT. On the other hand, SThM is a contact-mode scanning probe technique that uses a thermo-resistive probe sensitive to temperature changes on the surface of a sample with a spatial resolution of  $<100 \text{ nm}$ .<sup>34,35</sup> We use SThM to study the heating profile of biased devices in order to identify the thermal contribution of the CNT to the IMT of the VO<sub>2</sub>.

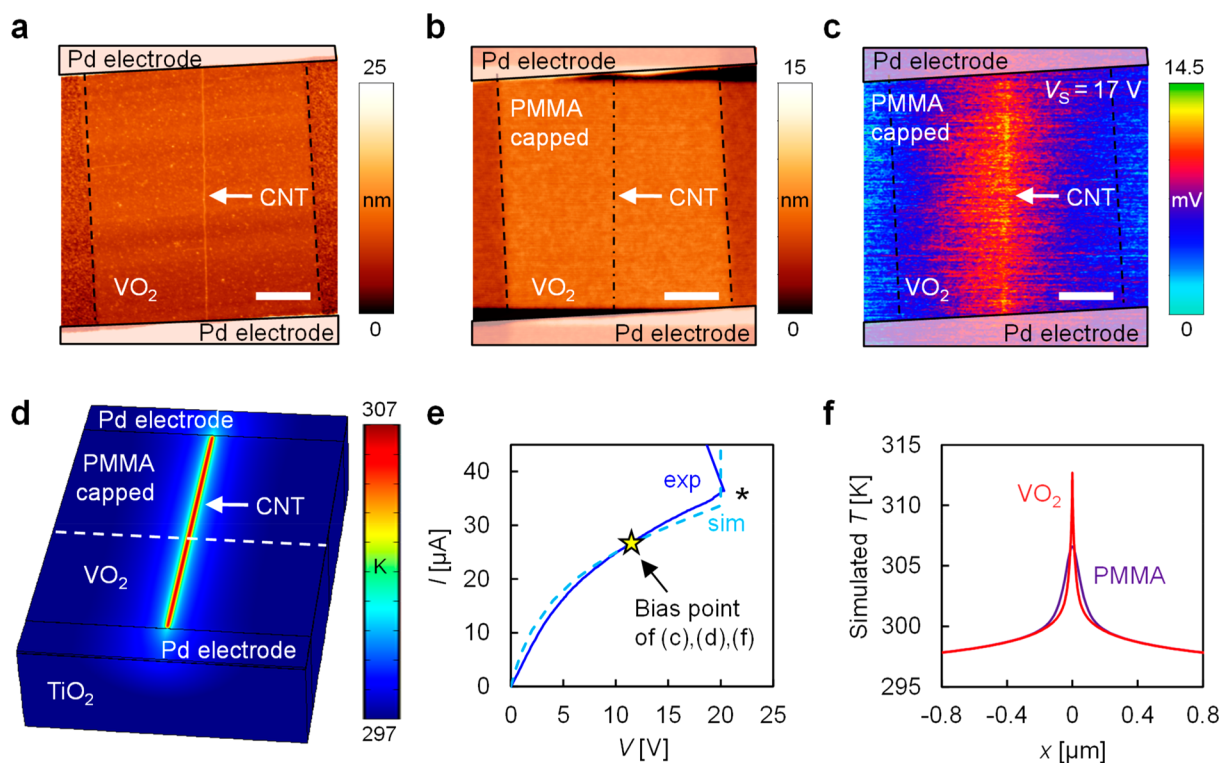


**Figure 4.** (a) Topography of an unbiased device with a single metallic CNT. (b) Topography of the same device covered by 50 nm of PMMA, with the CNT no longer visible. (c) SThM of the device under bias, prior to the metallic transition which occurs at  $V_S = 27$  V ( $V_{\text{IMT}} = 20.3$  V). (d) Simulated surface temperature on top of the PMMA, at the same device bias voltage. (e) Measured  $I$ - $V$  characteristics of the device (solid blue) compared to the model (dashed light blue), with switching marked by a \*. (f) Simulated temperature profile across the  $\text{VO}_2$  (red) and on the PMMA surface (purple) perpendicular to the CNT along the dashed white line in (d). The location of the CNT corresponds to the peak in  $\text{VO}_2$  temperature. Scale bars are  $1.5 \mu\text{m}$ .

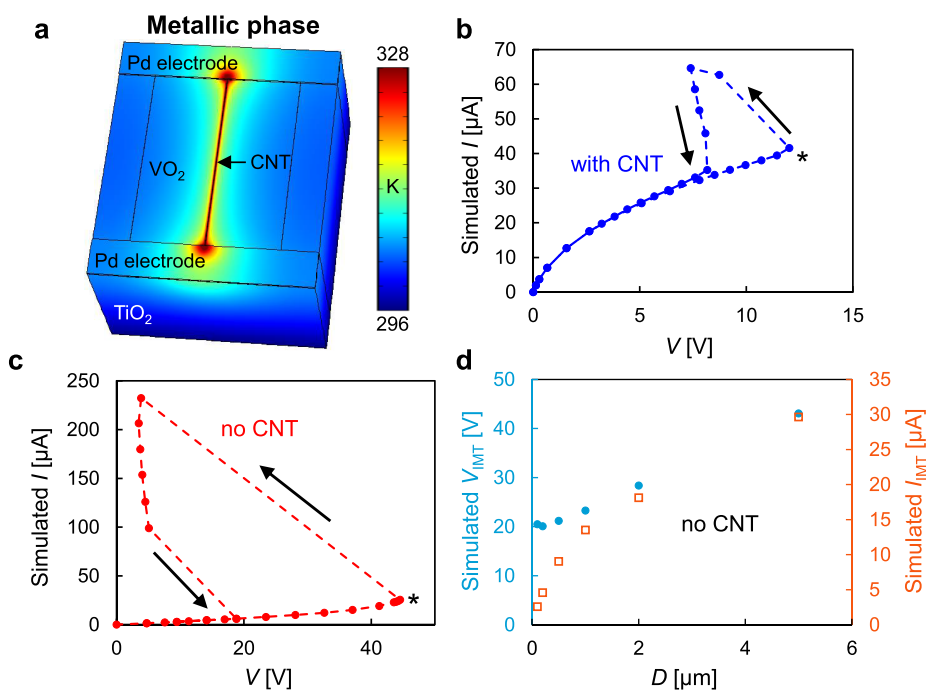
Figure 3a shows a topographic scan of a  $\text{VO}_2$  device without a CNT, and Figure 3b–d shows KPM results for that device, with applied voltages  $V_S$  as labeled. Scans are centered on the  $\text{VO}_2$  channel, with the  $\text{TiO}_2$  substrate revealed along the left and right edges. The small spots are carbon-based residue from processing. The contacts are just outside the scan with the grounded electrode at the top and the positive electrode at the bottom, connected to  $R_S = 200$  k $\Omega$  (see Figure 1g). Figure 3b shows a KPM scan with no bias across the device. The  $\text{VO}_2$  appears uniform, with a slight contrast against the process residues and  $\text{TiO}_2$ . Figure 3c,d shows KPM scans taken with a constant voltage  $V_S$  applied, (c) in the insulating state and (d) once the  $\text{VO}_2$  has electrically switched to the metallic state. In biased devices, there is a linear decrease in potential from the positive electrode to the grounded electrode (see Supporting Information Section 3). The scans have been processed with a first-order line flattening operation to remove this, highlighting local differences in surface potential across the device width. In both states, the device has for the most part a nearly uniform potential drop along it, with no strongly localized fields. In the metallic state, some slight variation exists across the width of the device from local differences in temperature and conductivity.

Figure 3e shows a topographic scan of a  $\text{VO}_2$  device with a CNT, and Figure 3f–h shows KPM results for the device, with potential variation across the width that differs significantly from the non-CNT device. The orientation of the electrodes relative to the images is the same, with the  $\text{VO}_2$  edges just outside the scan on the left/right. These images were processed in the same way. Although the raw potential drop

is linear, flattening reveals a small local concentration of the surface potential around the CNT in the insulating state (g). Once the device switches to the metallic state (h) and voltage snapback occurs, the flattened potential appears much more uniform across the device, with the CNT having little effect anymore.

The contrast in the potential across the devices with and without a CNT indicates that the CNT has a large impact on the  $\text{VO}_2$  switching. This could be a result of field enhancement or due to a thermally induced change in  $\text{VO}_2$  conductivity or workfunction. To test whether this can be attributed to thermal effects, we perform SThM on a similar  $\text{VO}_2$  device with a CNT. Figure 4a,b shows topographic scans of this device before and after capping with a 50 nm layer of poly(methyl methacrylate) (PMMA), with the CNT no longer visible after capping. This PMMA layer is needed for electrical insulation between the SThM probe and sample surface. The contacts are at the top and bottom of the image, and the device is held at a constant voltage,  $V_S = 17$  V, with  $R_S = 200$  k $\Omega$ . The SThM results in Figure 4c prior to switching confirm that there is significant localized heating around the CNT.

To quantify the local temperature rise in the  $\text{VO}_2$  induced by the CNT, we perform three-dimensional finite element simulations which self-consistently consider electrical, thermal, and Joule heating effects. The electrical conductivities of both the CNT and the  $\text{VO}_2$  are described as a function of temperature (Supporting Information Section 4). We also include electrical contact resistances and thermal boundary resistances, which cannot be neglected. The simulated device has the same dimensions as the real device scanned by SThM,



**Figure 5.** (a) Simulated temperature on the surface of a device with a CNT ( $L = 5 \mu\text{m}$ ,  $W = 4 \mu\text{m}$ ) after the metallic transition, with  $R_s = 200 \text{ k}\Omega$ . The color scale bar is cut off at  $T_{\text{IMT}} = 328 \text{ K}$  to highlight the switching region as dark red, but the central  $\text{VO}_2$  and CNT temperatures are higher. (b) Simulated  $I$ - $V$  curve of a device with a CNT using voltage control, including hysteresis. (c) Simulated  $I$ - $V$  curve of a device without a CNT using voltage control, including hysteresis. The switching voltage (\*) is much higher without the CNT to act as a heater. (d) Simulated switching voltage  $V_{\text{IMT}}$  and current  $I_{\text{IMT}}$  for devices without a CNT as the device dimensions  $D$  are reduced ( $L = W$  are simultaneously reduced).

capped by 50 nm of PMMA with a CNT at the device center. Simulating the device at the same bias as the SThM scan, we see in Figure 4d a similar temperature profile on the PMMA surface compared to the real device. Figure 4e shows that we can reproduce the experimental  $I$ - $V$  curve, with the simulated device having  $V_{\text{IMT}} \sim 20 \text{ V}$ . Figure 4f shows the simulated temperature profiles on the  $\text{VO}_2$  and PMMA surface at the SThM bias point, in the center of the device perpendicular to the CNT. The peak temperature in the  $\text{VO}_2$  directly underneath the CNT is higher and the temperature rise much more laterally confined than observed on the PMMA surface. Only a few-nanometer wide  $\text{VO}_2$  region under the CNT will reach  $T_{\text{IMT}}$  and trigger the transition, compared to nearly the entire device width when a CNT is not present (Supporting Information Figure S14a). The CNT itself is much hotter, reaching a temperature of  $\sim 400 \text{ K}$ , but the thermal boundary resistance (between CNT and  $\text{VO}_2$ ) and small contact area limit heat flow from the CNT to the  $\text{VO}_2$ .

When the series resistance  $R_s$  ( $= 200 \text{ k}\Omega$ ) is added to the model to limit positive feedback, the simulation can also reproduce switching to the metallic state, as shown in Figure 5a for a device with a CNT. These simulations show that the metallic  $\text{VO}_2$  forms a narrow conducting “filament,”  $\sim 10 \text{ nm}$  wide, just beneath the CNT. Switching is always triggered beneath the CNT regardless of its location in the  $\text{VO}_2$  channel, meaning that using a localized heater can provide a means of control over switching location. Full  $I$ - $V$  curves for both devices with (Figure 5b) and without (Figure 5c) a CNT can be simulated by sweeping the voltage, where the downward sweep uses the cooling branch of the  $R(T)$  curve (Figure 1i) to model hysteresis. Both curves reproduce experimental  $I$ - $V$  behavior remarkably well, including the differences in switch-

ing voltage and hysteresis between the two types of devices, using only Joule heating in the model and no other field effects. Thus, combined, our simulations, KPM, SThM, and electrical results suggest that Joule heating is a valid explanation for the mechanism of switching in our devices. Although a thermally assisted field mechanism cannot be excluded using our data (e.g., heating can increase carrier concentration to trigger a Mott transition or reduce the energy barrier for field-induced switching), Joule heating plays a key role in switching devices even in the narrow  $\text{VO}_2$  region activated by the hot CNT.

Using this electrothermal model, switching voltage  $V_{\text{IMT}}$  and current  $I_{\text{IMT}}$  can be simulated for  $\text{VO}_2$  devices without a CNT down to the nanoscale, shown in Figure 5d. The length and width of devices were simultaneously decreased, and a study of the separate effect of length and width may be found in the Supporting Information Section 4. As the device dimensions are reduced,  $I_{\text{IMT}}$  steadily decreases and so does  $V_{\text{IMT}}$  until becoming dominated by contact resistance to the narrow  $\text{VO}_2$  stripe. Combined, this results in a linear decrease of switching power  $P_{\text{IMT}}$  with device size. Adding a CNT to a nanoscale  $\text{VO}_2$  device would result in further reduction of  $V_{\text{IMT}}$  (especially if the contact resistance to the CNT is low and its heat transfer to the  $\text{VO}_2$  is efficient) while slightly increasing  $I_{\text{IMT}}$ , resulting in a similar overall switching power.

## CONCLUSIONS

In summary, we have shown that the IMT switching of  $\text{VO}_2$  can be triggered by nanoscale heaters made of individual metallic CNTs. Two-terminal  $\text{VO}_2$  devices with CNTs exhibit switching at less than half the voltage and power of traditional  $\text{VO}_2$  devices without a CNT, at all length scales. Using a combination of scanning probe techniques and finite element

simulations, we studied the origin and scale of the IMT in such devices with and without CNT heaters. Our results are consistent with a Joule heating mechanism in which the CNT locally heats the VO<sub>2</sub> and triggers IMT in a narrow region. These results highlight the importance of thermally engineering devices for low-power switching, by using confined heating in small volumes, and are also applicable to a wide variety of thermally activated phase-change and resistive switching devices.

## METHODS

Thin films of single crystalline VO<sub>2</sub> are epitaxially grown on TiO<sub>2</sub> (101) substrates using pulsed laser deposition (PLD), with a nominal thickness of 9 nm.<sup>28</sup> Separately, we grow aligned CNTs with an average diameter of 1.2 nm by chemical vapor deposition (CVD) on ST-cut quartz, then transfer them onto the VO<sub>2</sub>.<sup>27</sup> The CNTs on quartz were coated with 100 nm of Au by e-beam evaporation, onto which thermal release tape was pressed (Semiconductor Equipment Corp 1398MS, with adhesion 2.5 N/20 mm and release temperature 120 °C). The CNT/Au/tape stack was peeled off the quartz and then pressed onto the VO<sub>2</sub>. The tape was released on a hot plate at 130 °C, leaving behind the Au-coated CNTs on the VO<sub>2</sub> surface. An O<sub>2</sub> plasma clean (20 sccm, 25 mTorr, 55 W, 3 min) followed by an Ar plasma clean (15 sccm, 12.5 mTorr, 100 W, 3 min) were done to remove remaining tape adhesive on the Au, with the VO<sub>2</sub> protected from damage by the Au film. The remaining Au was removed using a KI wet etch, leaving behind aligned CNTs on the VO<sub>2</sub>. Some carbon-based residue is left after the transfer process (Figure 1e).

The VO<sub>2</sub> and CNTs were patterned into stripes of width  $W = 3\text{--}9\ \mu\text{m}$  using a photoresist etch mask. CNTs outside the VO<sub>2</sub> stripes were removed using a light O<sub>2</sub> plasma (20 sccm, 150 mTorr, 30 W, 1 min), then the VO<sub>2</sub> was wet etched for 30 s using a 25% nitric acid solution. Two-terminal devices were fabricated with 50 nm-thick Pd contact pads (with no Ti sticking layer) with dimensions  $300\ \mu\text{m} \times 250\ \mu\text{m}$  via e-beam evaporation and lift-off, with spacing (device lengths) ranging from  $L = 3$  to  $10\ \mu\text{m}$  (Figure 1g). Shorter devices with  $L = 300\ \text{nm}$  to  $2\ \mu\text{m}$  were made by adding small extensions of 50 nm-thick Pd to the existing pads using e-beam lithography (Figure 1h). Presence of metallic CNT(s) in devices was verified electrically and the number of CNTs confirmed by atomic force microscopy (AFM). The VO<sub>2</sub> film thickness after all processing and etching steps is  $\sim 5\ \text{nm}$  measured by AFM.

Electrical measurements are performed in a micromanipulator probe station from Janis Research, under vacuum ( $<10^{-4}$  Torr) with a Keithley 4200-SCS parameter analyzer applying a voltage  $V_S$ , all at room temperature ( $T_0 = 296\ \text{K}$ ) unless otherwise stated. A series resistance  $R_S = 20\ \text{k}\Omega$  and  $100\ \text{k}\Omega$  is used for short ( $<2\ \mu\text{m}$  long) devices with and without CNTs, respectively, and  $200\ \text{k}\Omega$  is used for all other devices. KPM is done on an Asylum Research system with a high-voltage module, while the device is biased at a constant voltage. Devices are coated with 50 nm-thick 2% 495 K PMMA in anisole to carry out passive-mode SThM measurements. PMMA is used rather than an oxide capping layer, because oxide deposition can reduce the stability of the CNT and VO<sub>2</sub>. The SThM tip (Pd on SiN, model PR-EX-GLA-5 from Anasys) is a thermo-resistive element sensitive to electrical discharges, so this capping is necessary in order to electrically isolate the tip from the device while it is biased. SThM is done in passive mode, with a 0.5 V set point and a 0.5 V tip bias.

## ASSOCIATED CONTENT

### Supporting Information

The Supporting Information is available free of charge on the ACS Publications website at DOI: 10.1021/acsnano.9b03397.

Additional details of CNT growth and VO<sub>2</sub> characterization, additional electrical measurements, discussion of device scaling, discussion of semiconducting and multi-CNT devices, discussion on the use of the series resistor,

discussion of contact resistance, additional KPM images, all COMSOL simulation details (PDF)

Movie illustrating the simulated temperature evolution in a VO<sub>2</sub> device with CNT during an  $I$ - $V$  curve (MP4)

## AUTHOR INFORMATION

### Corresponding Author

\*E-mail: [epop@stanford.edu](mailto:epop@stanford.edu).

### ORCID

Stephanie M. Bohachuk: 0000-0003-2705-4271

Miguel Muñoz Rojo: 0000-0001-9237-4584

Gregory Pitner: 0000-0002-0518-3745

Connor J. McClellan: 0000-0002-8733-9968

Eric Pop: 0000-0003-0436-8534

### Notes

The authors declare no competing financial interest.

## ACKNOWLEDGMENTS

The authors gratefully acknowledge Eilam Yalon and Suhas Kumar for commenting on the manuscript. This work was supported in part by the Stanford SystemX Alliance and by the National Science Foundation (NSF). Work was performed in part at the Stanford Nanofabrication Facility and the Stanford Nano Shared Facilities which receive funding from the NSF as part of the National Nanotechnology Coordinated Infrastructure award ECCS-1542152. S.B. acknowledges support from the Stanford Graduate Fellowship (SGF) program and the NSERC Postgraduate Scholarship program.

## REFERENCES

- (1) Imada, M.; Fujimori, A.; Tokura, Y. Metal-Insulator Transitions. *Rev. Mod. Phys.* **1998**, *70*, 1039–1263.
- (2) You, Z.; Ramanathan, S. Mott Memory and Neuromorphic Devices. *Proc. IEEE* **2015**, *103*, 1289–1310.
- (3) Berglund, C. N.; Guggenheim, H. J. Electronic Properties of VO<sub>2</sub> near the Semiconductor-Metal Transition. *Phys. Rev.* **1969**, *185*, 1022–1033.
- (4) Kakiuchida, H.; Jin, P.; Nakao, S.; Tazawa, M. Optical Properties of Vanadium Dioxide Film during Semiconductor-Metallic Phase Transition. *Jpn. J. Appl. Phys.* **2007**, *46*, L113–L116.
- (5) Jerry, M.; Shukla, N.; Paik, H.; Schlom, D. G.; Datta, S., Dynamics of Electrically Driven Sub-Nanosecond Switching in Vanadium Dioxide. Proceedings from the *IEEE Silicon Nanoelectron Workshop*, Honolulu, Hawaii, June 12–13; IEEE: New York, 2016.
- (6) Son, M.; Lee, J.; Park, J.; Shin, J.; Choi, G.; Jung, S.; Lee, W.; Kim, S.; Park, S.; Hwang, H. Excellent Selector Characteristics of Nanoscale VO<sub>2</sub> for High-Density Bipolar ReRAM Applications. *IEEE Electron Device Lett.* **2011**, *32*, 1579–1581.
- (7) Zhang, K.; Wang, B.; Wang, F.; Han, Y.; Jian, X.; Zhang, H.; Wong, H. VO<sub>2</sub>-Based Selection Device for Passive Resistive Random Access Memory Application. *IEEE Electron Device Lett.* **2016**, *37*, 978–981.
- (8) Pan, K.C.; Wang, W.; Shin, E.; Freeman, K.; Subramanyam, G. Vanadium Oxide Thin-Film Variable Resistor-Based RF Switches. *IEEE Trans. Electron Devices* **2015**, *62*, 2959–2965.
- (9) Shukla, N.; Thathachary, A. V.; Agrawal, A.; Paik, H.; Aziz, A.; Schlom, D. G.; Gupta, S. K.; Engel-Herbert, R.; Datta, S. A Steep-Slope Transistor Based on Abrupt Electronic Phase Transition. *Nat. Commun.* **2015**, *6*, 7812.
- (10) Vitale, W. A.; Casu, E. A.; Biswas, A.; Rosca, T.; Alper, C.; Krammer, A.; Luong, G. V.; Zhao, Q. T.; Mantl, S.; Schuler, A.; Ionescu, A. M. A Steep-Slope Transistor Combining Phase-Change and Band-to-Band-Tunneling to Achieve a Sub-Unity Body Factor. *Sci. Rep.* **2017**, *7*, 355.

- (11) Shukla, N.; Parihar, A.; Freeman, E.; Paik, H.; Stone, G.; Narayanan, V.; Wen, H.; Cai, Z.; Gopalan, V.; Engel-Herbert, R.; Schlom, D. G.; Raychowdhury, A.; Datta, S. Synchronized Charge Oscillations in Correlated Electron Systems. *Sci. Rep.* **2014**, *4*, 4964.
- (12) Yi, W.; Tsang, K. K.; Lam, S. K.; Bai, X.; Crowell, J. A.; Flores, E. A. Biological Plausibility and Stochasticity in Scalable VO<sub>2</sub> Active Memristor Neurons. *Nat. Commun.* **2018**, *9*, 4661.
- (13) Liu, L.; Kang, L.; Mayer, T. S.; Werner, D. H. Hybrid Metamaterials for Electrically Triggered Multifunctional Control. *Nat. Commun.* **2016**, *7*, 13236.
- (14) Kats, M. A.; Blanchard, R.; Genevet, P.; Yang, Z.; Qazilbash, M. M.; Basov, D. N.; Ramanathan, S.; Capasso, F. Thermal Tuning of Mid-Infrared Plasmonic Antenna Arrays Using a Phase Change Material. *Opt. Lett.* **2013**, *38*, 368–370.
- (15) Seo, M.; Kyoung, J.; Park, H.; Koo, S.; Kim, H. S.; Bernien, H.; Kim, B. J.; Choe, J. H.; Ahn, Y. H.; Kim, H. T.; Park, N.; Park, Q. H.; Ahn, K.; Kim, D. S. Active Terahertz Nanoantennas Based on VO<sub>2</sub> Phase Transition. *Nano Lett.* **2010**, *10*, 2064–2068.
- (16) Kats, M. A.; Blanchard, R.; Zhang, S.; Genevet, P.; Ko, C.; Ramanathan, S.; Capasso, F. Vanadium Dioxide as a Natural Disordered Metamaterial: Perfect Thermal Emission and Large Broadband Negative Differential Thermal Emittance. *Phys. Rev. X* **2013**, *3*, 041004.
- (17) Joushaghani, A.; Jeong, J.; Paradis, S.; Alain, D.; Stewart Aitchison, J.; Poon, J. K. S. Voltage-Controlled Switching and Thermal Effects in VO<sub>2</sub> Nano-Gap Junctions. *Appl. Phys. Lett.* **2014**, *104*, 221904.
- (18) Radu, I. P.; Govoreanu, B.; Mertens, S.; Shi, X.; Cantoro, M.; Schaekers, M.; Jurczak, M.; De Gendt, S.; Stesmans, A.; Kittl, J. A.; Heyns, M.; Martens, K. Switching Mechanism in Two-Terminal Vanadium Dioxide Devices. *Nanotechnology* **2015**, *26*, 165202.
- (19) Aetukuri, N. P. B. The Control of Metal-Insulator Transition in Vanadium Dioxide. *Ph.D. Thesis*, Stanford University, 2013, <https://searchworks.stanford.edu/view/10163818>.
- (20) Raoux, S.; Xiong, F.; Wuttig, M.; Pop, E. Phase Change Materials and Phase Change Memory. *MRS Bull.* **2014**, *39*, 703–710.
- (21) Xiong, F.; Liao, A. D.; Estrada, D.; Pop, E. Low-Power Switching of Phase-Change Materials with Carbon Nanotube Electrodes. *Science* **2011**, *332*, 568–570.
- (22) Li, D.; Sharma, A. A.; Gala, D. K.; Shukla, N.; Paik, H.; Datta, S.; Schlom, D. G.; Bain, J. A.; Skowronski, M. Joule Heating-Induced Metal-Insulator Transition in Epitaxial VO<sub>2</sub>/TiO<sub>2</sub> Devices. *ACS Appl. Mater. Interfaces* **2016**, *8*, 12908–12914.
- (23) Stefanovich, G.; Pergament, A.; Stefanovich, D. Electrical Switching and Mott Transition in VO<sub>2</sub>. *J. Phys.: Condens. Matter* **2000**, *12*, 8837–8845.
- (24) Chen, F. H.; Fan, L. L.; Chen, S.; Liao, G. M.; Chen, Y. L.; Wu, P.; Song, L.; Zou, C. W.; Wu, Z. Y. Control of the Metal-Insulator Transition in VO<sub>2</sub> Epitaxial Film by Modifying Carrier Density. *ACS Appl. Mater. Interfaces* **2015**, *7*, 6875–6881.
- (25) Liao, A.; Alizadegan, R.; Ong, Z.-Y.; Dutta, S.; Xiong, F.; Hsia, K. J.; Pop, E. Thermal Dissipation and Variability in Electrical Breakdown of Carbon Nanotube Devices. *Phys. Rev. B* **2010**, *82*, 205406.
- (26) Xiong, F.; Liao, A.; Pop, E. Inducing Chalcogenide Phase Change with Ultra-Narrow Carbon Nanotube Heaters. *Appl. Phys. Lett.* **2009**, *95*, 243103.
- (27) Patil, N.; Lin, A.; Myers, E. R.; Koungmin, R.; Badmaev, A.; Chongwu, Z.; Wong, H. S. P.; Mitra, S. Wafer-Scale Growth and Transfer of Aligned Single-Walled Carbon Nanotubes. *IEEE Trans. Nanotechnol.* **2009**, *8*, 498–504.
- (28) Jeong, J.; Aetukuri, N.; Graf, T.; Schladt, T. D.; Samant, M. G.; Parkin, S. S. Suppression of Metal-Insulator Transition in VO<sub>2</sub> by Electric Field-Induced Oxygen Vacancy Formation. *Science* **2013**, *339*, 1402–1405.
- (29) Pop, E.; Mann, D. A.; Goodson, K. E.; Dai, H. Electrical and Thermal Transport in Metallic Single-Wall Carbon Nanotubes on Insulating Substrates. *J. Appl. Phys.* **2007**, *101*, 093710.
- (30) Martens, K.; Radu, I. P.; Mertens, S.; Shi, X.; Nyns, L.; Cosemans, S.; Favia, P.; Bender, H.; Conard, T.; Schaekers, M.; De Gendt, S.; Afanas'ev, V.; Kittl, J. A.; Heyns, M.; Jurczak, M. The VO<sub>2</sub> Interface, the Metal-Insulator Transition Tunnel Junction, and the Metal-Insulator Transition Switch On-Off Resistance. *J. Appl. Phys.* **2012**, *112*, 124501.
- (31) Percy, R.; Kittiwatanakul, S.; Lu, J.; Stan, M.; Wolf, S.; Weikle, R. M. Method for Characterizing the Contact Resistance of Metal-Vanadium Dioxide Thin Film Interfaces. *Appl. Phys. Lett.* **2014**, *105*, 021603.
- (32) Jeong, J.; Yong, Z.; Joushaghani, A.; Tsukernik, A.; Paradis, S.; Alain, D.; Poon, J. K. Current Induced Polycrystalline-to-Crystalline Transformation in Vanadium Dioxide Nanowires. *Sci. Rep.* **2016**, *6*, 37296.
- (33) Sadewasser, S.; Glatzel, T. *Kelvin Probe Force Microscopy: Measuring and Compensating Electrostatic Forces*; Springer: Heidelberg, 2011.
- (34) Borca-Tasciuc, T. Scanning Probe Methods for Thermal and Thermoelectric Property Measurements. *Annu. Rev. Heat Transfer* **2013**, *16*, 211–258.
- (35) Yalon, E.; Deshmukh, S.; Munoz Rojo, M.; Lian, F.; Neumann, C. M.; Xiong, F.; Pop, E. Spatially Resolved Thermometry of Resistive Memory Devices. *Sci. Rep.* **2017**, *7*, 15360.

#### NOTE ADDED AFTER ASAP PUBLICATION

The paper was published ASAP on August 26, 2019 with an error in equation S4 in the Supporting Information. The corrected version was reposted on August 26, 2019.

# Localized Triggering of the Insulator-Metal Transition in VO<sub>2</sub> Using a Single Carbon Nanotube

Stephanie M. Bohachuk,<sup>1</sup> Miguel Muñoz Rojo,<sup>1,2</sup> Gregory Pitner,<sup>1</sup> Connor J. McClellan,<sup>1</sup> Feifei Lian,<sup>1</sup> Jason Li,<sup>3</sup> Jaewoo Jeong,<sup>4</sup> Mahesh G. Samant,<sup>4</sup> Stuart S. P. Parkin,<sup>4</sup> H.-S. Philip Wong,<sup>1</sup> Eric Pop<sup>1,5,\*</sup>

<sup>1</sup>Dept. of Electrical Engineering, Stanford University, Stanford, CA 94305, USA

<sup>2</sup>Dept. of Thermal and Fluid Engineering, University of Twente, 7500 AE Enschede, The Netherlands

<sup>3</sup>Asylum Research, Santa Barbara, CA 93117, USA

<sup>4</sup>IBM Almaden Research Center, San Jose, CA 95120, USA

<sup>5</sup>Dept. of Materials Science and Engineering, Stanford University, Stanford, CA 94305, USA

\*Contact: [epop@stanford.edu](mailto:epop@stanford.edu)

## **Supplementary Information Content:**

1. VO<sub>2</sub> Characterization and CNT Growth
2. Electrical Measurements of Devices
  - a. Additional Electrical Characterization
  - b. Semiconducting and Multi-CNT Devices
  - c. Temperature Dependence
  - d. Contact Resistance
  - e. Series Resistance and Burn-in
  - f. Switching Field
3. Kelvin Probe Microscopy
4. Three-Dimensional Finite Element Simulations
  - a. Model Details
  - b. Simulated Device Scaling
  - c. Models Using Other Mechanisms
5. Supplementary Video
6. Supplementary References

## 1. VO<sub>2</sub> Characterization and CNT Growth

VO<sub>2</sub> thin films 9 nm thick were deposited using pulsed laser deposition on 1 cm<sup>2</sup> single crystal TiO<sub>2</sub> (101) pieces.<sup>1</sup> As-deposited VO<sub>2</sub> films were smooth with an rms roughness of ~1 Å. X-ray photoelectron spectroscopy (XPS) indicated the presence of a very thin surface oxidation, likely V<sub>2</sub>O<sub>5</sub> (Figure S1).

Separately, horizontally aligned single-wall carbon nanotubes (CNTs) were grown *via* chemical vapor deposition (CVD) on ST-cut quartz using an ethanol source, which resulted in CNTs with an average diameter of 1.2 nm.<sup>2</sup> The CNTs grew perpendicular to patterned stripes of 1.3 Å thick Fe catalyst nanoparticles, resulting in a mixture of semiconducting and metallic CNTs with a random spacing between them, on average 0.3 CNT/μm. This density was chosen so that fabricating 3 to 9 μm wide VO<sub>2</sub> channels would result in a mixture of devices with no CNT, a single CNT, and multiple CNTs.

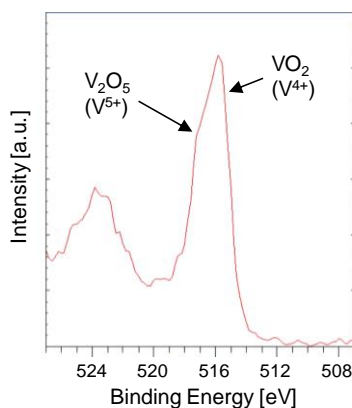


**Figure S1.** X-ray photoelectron spectroscopy (XPS) of the VO<sub>2</sub> film prior to processing, with V2p3 peaks indicating a VO<sub>2</sub> composition with a slight surface oxidation.

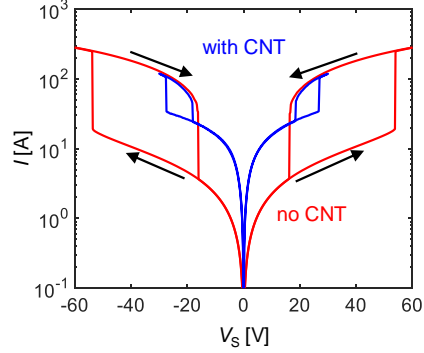
## 2. Electrical Measurements of Devices

### 2a. Additional Electrical Characterization

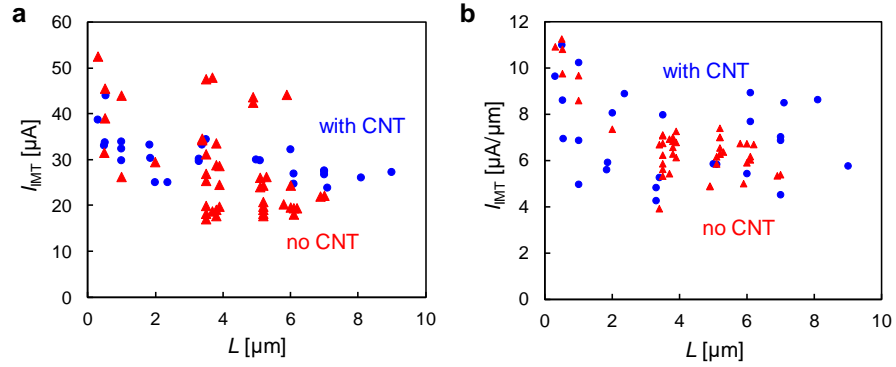
Measurements shown were all performed under vacuum ( $< 10^{-4}$  Torr), removing potential effects of atmosphere or water vapour on the CNTs. However, measurements can safely be done in air and yield similar results. Figure S2 shows that devices have the same switching voltage and  $I$ - $V$  characteristics regardless of bias polarity. Conduction is linear at low bias in either direction, suggesting ohmic contacts.

Figure S3 shows that the threshold current ( $I_{MT}$ ) for most devices (with or without a CNT) falls roughly in the same range. For devices without a CNT, switching depends on the VO<sub>2</sub> heating that occurs throughout the entire volume. In other words, *without* a CNT the threshold current would be higher in thicker or wider VO<sub>2</sub> devices (due to larger VO<sub>2</sub> volume) and higher in shorter VO<sub>2</sub> devices (due to heat loss to the contacts). These trends can be seen in the spread of  $I_{MT}$  for devices with VO<sub>2</sub> of different widths but without a CNT, in Figure S3a, as well as in Figure S15. However, most of our experimental devices had the same VO<sub>2</sub> thickness and nearly the same VO<sub>2</sub> widths, thus not much variation is seen in their threshold currents. In devices *with* a CNT we expect the switching current to be independent of VO<sub>2</sub> width, because the narrow CNT triggers the same heating regardless of the width of the VO<sub>2</sub> stripe underneath. The switching *voltage* of VO<sub>2</sub> devices with a CNT is lower because initially the current flows mostly in the CNT, which heats up more easily. Figure S3b shows switching current normalized by VO<sub>2</sub> width, which is appropriate for devices without a CNT but adds spread in the  $I_{MT}$  of devices with a CNT.

A slight increase in device switching voltage ( $V_{\text{IMT}}$ ) is observed in narrow devices without a CNT, as shown in Figure S4a (accompanying simulations are in Section 4b). After burn-in, which is larger for narrower devices (Section 2e),  $V_{\text{IMT}}$  has a much weaker width dependence across the range of device widths measured (3 to 9  $\mu\text{m}$ ). As the  $\text{VO}_2$  width is reduced the switching current and power decrease slightly, shown in Figure S4b and S4c, respectively. In contrast, devices with a CNT show no dependence of  $V_{\text{IMT}}$  on  $\text{VO}_2$  width, and depend solely on the CNT quality and the efficiency of heat transfer to the  $\text{VO}_2$ .



**Figure S2.** Forward and reverse DC voltage-controlled switching of devices with ( $L = 6 \mu\text{m}$ ,  $W = 2.9 \mu\text{m}$ ) and without a CNT ( $L = 6 \mu\text{m}$ ,  $W = 5.1 \mu\text{m}$ ), showing switching is independent of polarity.



**Figure S3.** (a) Total current just prior to switching ( $I_{\text{IMT}}$ ) for devices with (blue circles) and without (red triangles) a CNT, for a variety of widths ( $W = 3$  to  $9 \mu\text{m}$ ). (b)  $I_{\text{IMT}}$  normalized by  $\text{VO}_2$  width  $W$ , for devices with (blue circles) and without (red triangles) a CNT.

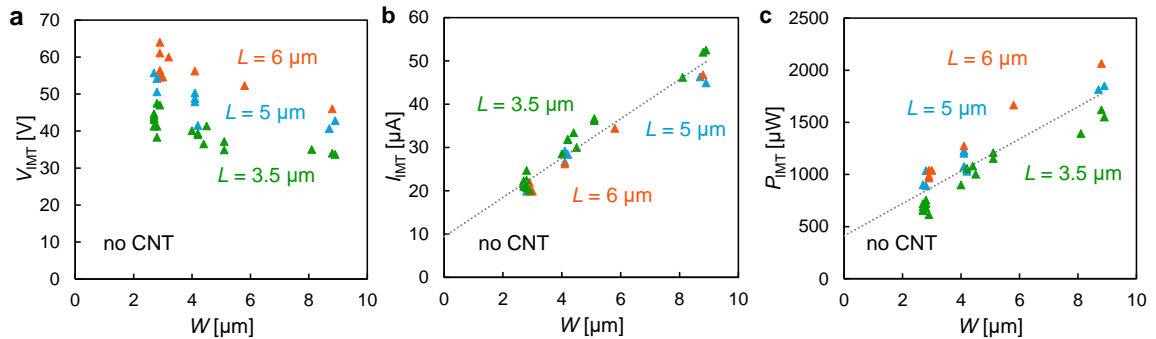


**Figure S4.** (a) Switching voltage  $V_{\text{IMT}}$  for devices without a CNT is higher in narrower devices during the first switching event. After burn-in (Section 2e),  $V_{\text{IMT}}$  shows a much weaker trend with width. (b) Switching current  $I_{\text{IMT}}$  for devices without a CNT scales linearly with width. (c) Switching power of devices without a CNT is lower in narrower devices. Dashed lines show linear fits.

## 2b. Semiconducting and Multi-CNT Devices

The CNT growth conditions on quartz generate a mixture of semiconducting and metallic CNTs. In addition, because the spacing between parallel CNTs is uneven, our process ultimately yields a range of VO<sub>2</sub> devices with semiconducting CNT(s), with metallic CNT(s), with a mixture of both, or with no CNTs. The presence of metallic or “weakly metallic” CNT(s) was determined by the current carried in two-terminal electrical measurements, and the number of CNTs was confirmed by atomic force microscopy (AFM). A metallic CNT carries considerably more current and will show evidence of sublinear  $I$ - $V$  behaviour (typically beyond  $\sim 3$  V when  $L \sim$  a few microns) and current saturation at higher voltages (typically near 10 to 25  $\mu$ A).<sup>3</sup> Weakly metallic CNTs (damaged or poorly contacted metallic CNTs, or CNTs with a small band gap) are less conductive and often without clear saturation. Semiconducting CNTs carry much less current (typically  $\ll 1$   $\mu$ A ungated), and their presence was verified through AFM. Examples of metallic and “weakly metallic” CNT  $I$ - $V$  characteristics are shown in Figure S5a, with CNT devices fabricated in a similar manner but on TiO<sub>2</sub> (101) with no VO<sub>2</sub> film present (the substrate is insulating). Although the focus of this study was on devices with single metallic CNTs, the switching behaviours of several other types of devices were also measured. Figure S5b shows the switching voltages ( $V_{\text{IMT}}$ ) of 112 devices, including devices with CNT(s) (filled circles) and without (open triangles).

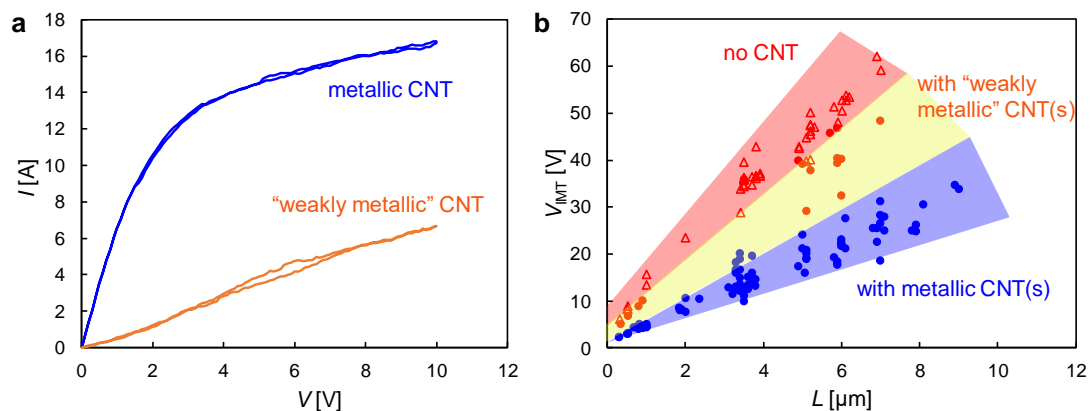


**Figure S5.** (a) Example  $I$ - $V$  curves of devices ( $L \sim 4$   $\mu$ m) with metallic and “weakly metallic” CNTs on TiO<sub>2</sub> (no VO<sub>2</sub> film). (b) Switching voltage  $V_{\text{IMT}}$  as a function of length (contact separation) for devices with no CNT (open triangles) and at least one CNT (filled circles). Devices with  $I$ - $V$  curves that indicate the presence of metallic CNT(s) are in blue, and those without are in red. Those that show a “weakly metallic” CNT presence in their  $I$ - $V$  characteristics (orange) have a switching voltage in between the two groups.

Devices with a semiconducting CNT (red circles) have the same switching voltage as devices without any CNTs (red triangles). These devices are electrically indistinguishable from each other, because the ungated semiconducting CNTs do not carry sufficiently high currents to induce heating in the VO<sub>2</sub>.

Devices with multiple metallic CNTs switch at the same voltage as those with single metallic CNTs (both blue circles). This suggests that the transition is triggered by the “best” (*i.e.* most conductive) metallic CNT, which heats up the most. After the VO<sub>2</sub> voltage snapback (due to the series resistor  $R_s$ ) the CNTs no longer carry enough current to trigger further IMT, so any benefit to having multiple CNTs is lost. Note that all our devices have CNTs spaced far apart ( $\sim 0.3$   $\mu$ m on average), and thus each CNT acts independently from one another. If the metallic CNTs are spaced much closer,  $V_{\text{IMT}}$  may be further reduced.

A weakly metallic CNT (orange circles) may still carry enough current to trigger IMT in the VO<sub>2</sub>, with  $V_{\text{IMT}}$  between that of a device with a good metallic CNT (blue) and one without any CNT at all (red).

## 2c. Temperature Dependence

As expected,  $V_{\text{IMT}}$  reduces as the ambient temperature ( $T_0$ ) increases, which is set by the stage temperature. This is because less power is needed to raise the device temperature to  $T_{\text{IMT}}$ . This is true both for devices with (Figure S6a) and without a CNT. The switching field  $E_{\text{IMT}}$  (extracted from a linear fit to  $V_{\text{IMT}}$  vs  $L$ ) decreases for both types of devices as the temperature increases, as shown in Figure S6b. If the ambient temperature is high enough (above or at  $T_{\text{MIT}}$ ), then the device will remain metallic after the bias is removed due to hysteresis in the  $\text{VO}_2$ . At all temperatures, the switching field for devices with a CNT is less than half that required for devices without a CNT.  $E_{\text{IMT}}$  for a device with a CNT at 296 K is slightly below that of a device without a CNT at 320 K, suggesting that the CNT heats the  $\text{VO}_2$  to at least 320 K.

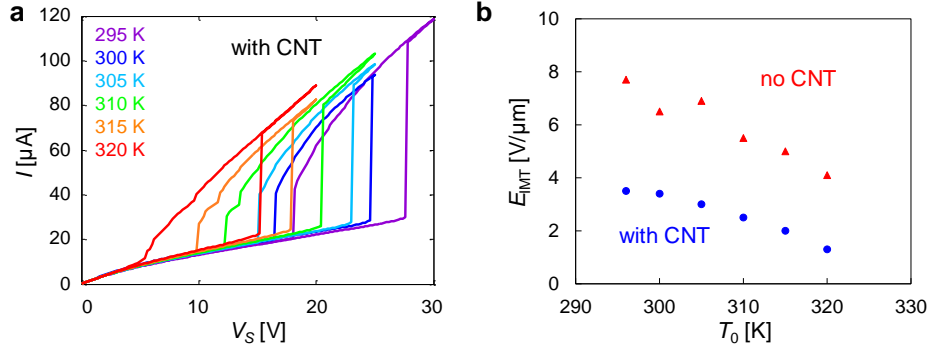


**Figure S6.** (a) Switching of a device with a CNT ( $L = 5 \mu\text{m}$ ,  $W = 5.1 \mu\text{m}$ ) using DC voltage control, showing reduced switching voltage as the stage temperature increases. (b) The effective switching field  $E_{\text{IMT}}$  lowers as temperature is increased, for both devices with (blue circles) and without (red triangles) a CNT.  $E_{\text{IMT}}$  is extracted as the slope of a linear fit to  $V_{\text{IMT}}$  vs.  $L$  at each stage temperature.

## 2d. Contact Resistance

An estimate of the contact resistance  $R_C$  between Pd and insulating  $\text{VO}_2$  can be obtained using the transfer length method (TLM), shown in Figure S7. The y-intercept corresponds to  $2R_C$  and the slope corresponds to the sheet resistance  $R_{\text{sh}}$ . The devices are spread across the chip and have different widths, resulting in significant spread in their resistance since the cleanliness and contact quality can vary, as well as to a lesser extent the  $\text{VO}_2$  resistivity and thickness. We get a value for  $R_{\text{sh}}$  of  $2520 \pm 150 \text{ k}\Omega$ , and a value for  $R_C$  of  $460 \pm 330 \text{ k}\Omega \cdot \mu\text{m}$  or equivalently, a contact resistivity  $\rho_c \sim (0.8 \pm 0.3) \times 10^{-3} \Omega \cdot \text{cm}^2$ . For a typical  $5 \mu\text{m}$  wide device, this gives a contact resistance of  $92 \pm 66 \text{ k}\Omega$ .

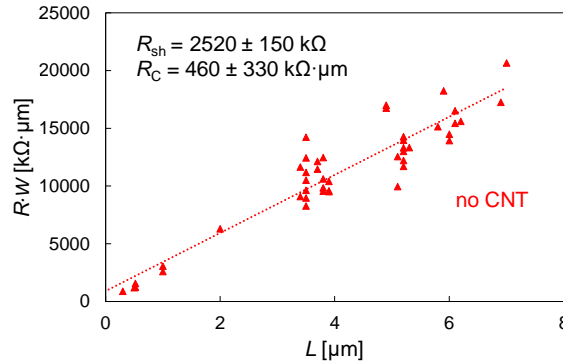


**Figure S7.** Insulating state resistance for  $\text{VO}_2$  devices without a CNT as a function of length. The vertical axis intercept gives an estimate of twice the device contact resistance ( $2R_C$ ), and the slope gives an estimate for sheet resistance ( $R_{\text{sh}}$ ).

## 2e. Series Resistance and Burn-in

A series resistor ( $R_S$ ) is necessary to protect devices from overheating failure in the metallic state (the heat can melt the contacts). The value should be chosen low enough to not affect  $V_{\text{IMT}}$  (a small fraction of the high-resistance insulating state), but high enough to prevent permanent damage in the metallic state (higher than the low-resistance metallic state). There is no one correct value for  $R_S$  and a range of values can be used, as shown in Figure S8a. Using a larger  $R_S$  reduces the metallic state current, thus limiting the on/off ratio. There is a slight increase in the total applied voltage ( $V_S$ ) required to switch the device but  $V_{\text{IMT}}$  does not change, as shown in Figure S8b. As device dimensions are reduced, power dissipation in the metallic state reduces because  $V_{\text{IMT}}$  decreases. Thus, shorter devices do not need as high a value of  $R_S$  for protection.

Figure S8c shows that similar trends are observed for a  $\text{VO}_2$  device with a CNT heater. However, when higher values of  $R_S$  are used, the transition shows an increasingly long period of slow increase in current, corresponding to oscillations, followed by a smaller abrupt transition. The CNT triggers switching in the  $\text{VO}_2$ , but the subsequent reduction in voltage across the device means there is not enough power needed to remain metallic (the CNT and  $\text{VO}_2$  cool) so the  $\text{VO}_2$  returns to insulating, where the CNT heating is again able to switch the  $\text{VO}_2$ , and the system repeatably cycles between IMT and MIT.

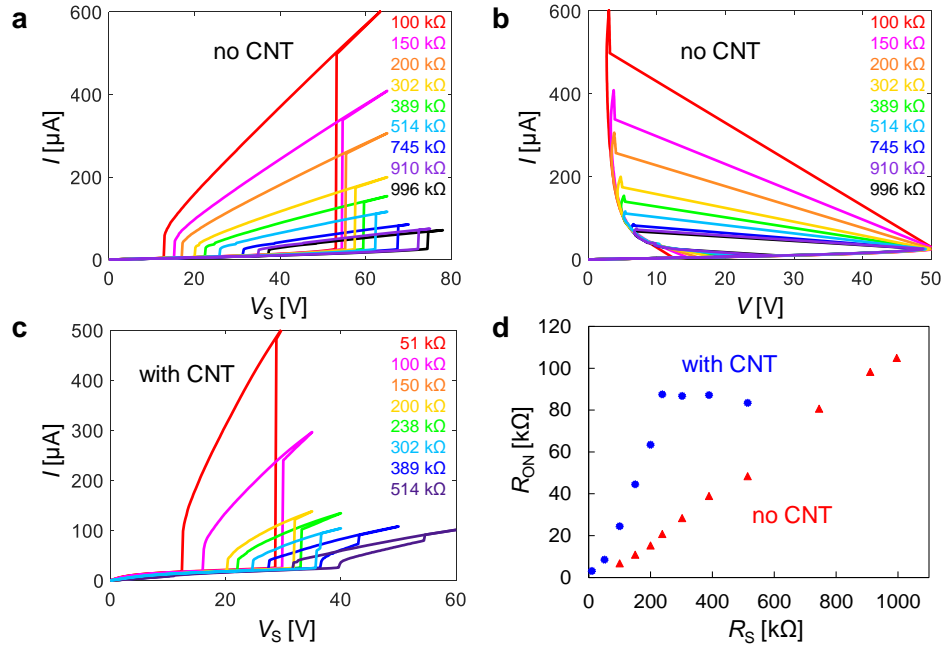
Figure S8d shows that as  $R_S$  increases, the metallic state resistance ( $R_{\text{ON}}$ ) of the device increases (calculated just after switching, with  $R_S$  subtracted out). This indicates that increasing  $R_S$  reduces the steady state volume of the metallic region or “filament”, consistent with prior work.<sup>4</sup> As a secondary effect this change in  $R_{\text{ON}}$  could be partly due to the metallic state’s temperature coefficient of resistance (TCR), since changing  $R_S$  changes the device temperature. In devices with a CNT,  $R_{\text{ON}}$  plateaus when devices show oscillatory behaviour (where  $R_{\text{ON}}$  is determined just after the final abrupt transition). This may indicate that there is a minimum width (a minimum metallic state power) required for the metallic “filament” to be stable.

Figure S9a shows where we attach the series resistor  $R_S$ , at the base of the probe tip, to avoid excess cable connections. The location of this resistor is important as well as its value. The abrupt change in device resistance triggers a large transient current due to capacitors discharging that are in parallel with the device (since  $I = C dV/dt$ ).<sup>5,6</sup> This includes intrinsic device capacitance as well as other parasitic capacitances from the contacts and measurement setup such as probe pad capacitance (pad-to-pad or through the  $\text{TiO}_2$  substrate to the stage) or coax cable capacitance.  $R_S$  should be physically close to the device, because then only the device capacitances see the change in conductance (the resistor shields the device from the other external capacitors). A better choice would be to use an integrated on-chip resistor (or transistor, for a variable  $R_S$  with smaller area) as a current limiter directly connected to the  $\text{VO}_2$  device, however our choice in Figure S9a is the best practical one, given the setup.

A typical current overshoot event at the IMT is shown in Figure S9b for a device without a CNT, measured using a  $50 \Omega$  oscilloscope in series with the device. Although the overshoot lasts less than 100 ns, the current can transiently reach up to a few mA, which is significant compared to the few hundred  $\mu\text{A}$  which is limited by  $R_S$  when the device is in the metallic state. The overshoot duration is smaller in shorter devices. Overshoot also occurs on a similar time scale for devices with a CNT, but with a reduced magnitude.

Devices without a CNT show a burn-in effect, displayed in Figure S9c, with the first switching occurring at a slightly higher  $V_{\text{IMT}}$  than all subsequent switching. This difference is typically on the order of 0.2 – 4 V and is generally higher in narrower devices. This burn-in also results in a slight increase in insulating state conductivity. Burn-in may be a result of the heat from current overshoot at the moment of switching, which could cause a subtle change in the  $\text{VO}_2$  or the contacts (such as breaking through the native surface oxide or annealing the contacts), making it slightly easier to repeat switching. Devices typically recover

from burn-in (if measured again another day then switching voltage has shifted back up for the first switching event, and the device experiences burn-in again). All other switching voltages, currents, and  $I$ - $V$  characteristics reported are after this initial burn-in. Burn-in is not observed in devices with a CNT and is reduced in short devices without a CNT because of the lower switching power and current overshoot.



**Figure S8.** (a) DC voltage-controlled switching of a  $\text{VO}_2$  device without a CNT ( $L = 5.1 \mu\text{m}$ ,  $W = 4.1 \mu\text{m}$ ) for different values of  $R_S$ , plotting total applied voltage  $V_S$ . (b) The same  $I$ - $V$  measurements as in (a) plotted with the voltage across the device. The choice of  $R_S$  does not impact  $V_{\text{IMT}}$ . (c) DC voltage-controlled switching of a device with a CNT ( $L = 7.1 \mu\text{m}$ ,  $W = 2.8 \mu\text{m}$ ) for different  $R_S$ . (d) Device resistance just after switching ( $R_{\text{ON}}$ ), as a function of  $R_S$  for the same devices, without (red triangles) and with a CNT (blue circles).  $R_S$  can be used to control the metallic state “filament” width.

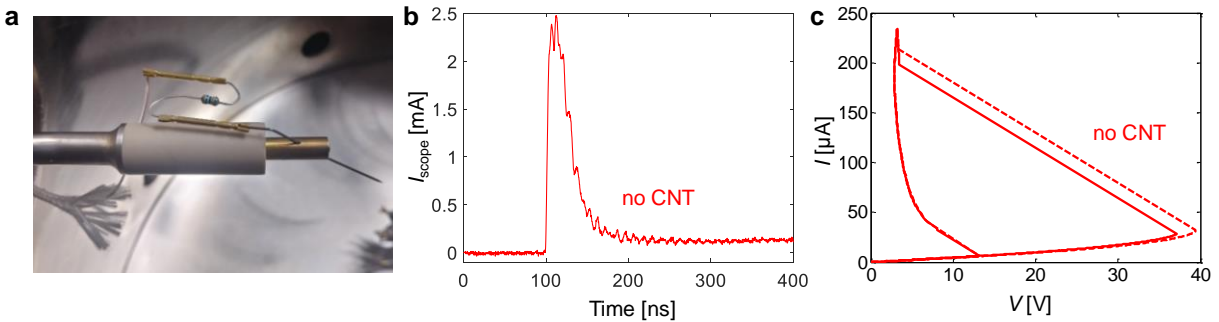


**Figure S9.** (a) Setup for using a series resistor  $R_S$  as current compliance, with  $R_S$  on the probe tip, as close as possible to the device under test. (b) Typical current overshoot when a device without a CNT switches ( $L = 3.5 \mu\text{m}$ ,  $W = 2.7 \mu\text{m}$ ), due to capacitive discharge. The current is measured using a  $50 \Omega$  oscilloscope in series with the device. Devices with a CNT also show current overshoot waveforms with a nearly identical shape and time-scale, but with a reduced magnitude. (c) DC voltage-controlled switching of a device without a CNT ( $L = 3.8 \mu\text{m}$ ,  $W = 5.1 \mu\text{m}$ ) on the first sweep (dashed), and subsequent sweeps (solid). There is a slight shift (a “burn-in”) in  $V_{\text{IMT}}$  after the first switching event.

## 2f. Switching Field

Thermally triggered switching occurs when the steady state temperature in the device (or some part of it) reaches the insulator-metal transition temperature ( $T_{\text{IMT}}$ ). According to a very simple Joule heating description of a  $\text{VO}_2$  block on a substrate, the input electrical power  $P = V^2/R$  causes the temperature to rise with a maximum determined by the thermal conductance to the surrounding environment  $G_{\text{th}}$ :

$$\frac{V^2}{R} = G_{\text{th}}(T_{\text{IMT}} - T_0) \quad (1)$$

If we write an effective switching field  $E_{\text{IMT}} = V/L$ , where  $V$  is the voltage across the  $\text{VO}_2$  length  $L$  at the transition (excluding the voltage drop at the contacts), then the field could be described as:<sup>6</sup>

$$E_{\text{IMT}} = \sqrt{\frac{G_{\text{th}}R(T_{\text{IMT}} - T_0)}{L^2}} \quad (2)$$

This does not capture aspects of real devices like the contacts and non-uniform heating. However, it is useful in pointing out some dependencies of the switching field. *Via*  $G_{\text{th}}$  the switching field depends on the thermal boundary resistance to the substrate, the thermal conductivity of the substrate, the geometry, and the resistivity of the  $\text{VO}_2$ . Two-terminal devices can vary in this regard, making it hard to give a direct comparison of switching field. Table 1 lists switching fields of two-terminal switching devices extracted from literature with a similar change in temperature to our work ( $\Delta T = T_{\text{IMT}} - T_0 \approx 32$  K). Fields are listed as a slope (with a vertical axis intercept  $V_{\text{offset}}$  due to heat loss and resistance at the contacts) or as a long channel  $V/L$  where  $L$  is at least a few microns long. We note that thicker, wider  $\text{VO}_2$  devices (lower  $R$ ) on better thermal insulating substrates (lower  $G_{\text{th}}$ ) typically have lower switching field  $E_{\text{IMT}}$ .

**Table 1.** Switching Fields in Prior  $\text{VO}_2$  Films

Ref.	Deposition Technique	Substrate	$L$ ( $\mu\text{m}$ )	$W$ ( $\mu\text{m}$ )	$t$ (nm)	Contact	$E_{\text{IMT}}$ (V/ $\mu\text{m}$ )	$V_{\text{offset}}$ (V)	$\Delta T$ (K)
7	PLD	$\text{TiO}_2$ (001)	0.02 – 0.11	1	10	Ta/Au	13	0.1	35
8	MBE	$\text{TiO}_2$ (001)	6	10	10	Pd/Au	2.2	-	35
9	PLD	$\text{SiO}_2$ (300 nm)	2, 10	20	100	Cr/Cu/Au	1.2 – 4.3 <sup>a</sup>	-	51
10	sputtered	$\text{SiO}_2$ (2 $\mu\text{m}$ )	0.1 – 1	10	100	Ag, Cu, Au, Pd	2.0 – 2.3 <sup>b</sup>	2.2 – 3.3 <sup>b</sup>	45
11	sputtered	$\text{SiO}_2$ (500 nm)	7.5	50	360	Al	0.5	-	34
12	sputtered	$\text{SiO}_2$ (100 nm)	4	4	100	Pd/Au	1.2	-	28
13	oxidation	poly- $\text{Al}_2\text{O}_3$ (20 nm)	0.1 – 5	2, 10	100	Ti/Au	17.4	4.1	53
4	oxidation	$\text{Al}_2\text{O}_3$ (11 $\bar{2}$ 0)	5 – 80	100	200	Cr/Au	2.9 2.2	24.4 22.0	37 27
14	PLD	$\text{Al}_2\text{O}_3$ (1102)	5	50	90	Cr/Au	2.3, 3.4 <sup>c</sup>	-	32
15	sputtered	$\text{Al}_2\text{O}_3$ (10 $\bar{1}$ 0)	20	100	100	Ni	1.0	-	45
16	sputtered	$\text{Al}_2\text{O}_3$ (r-cut)	20	50	130	Au	2.6	-	18
17	sol-gel	$\text{Al}_2\text{O}_3$	10	10	100	Ni	1.0	-	45

<sup>a</sup>different contact geometries, <sup>b</sup>different contact metals, <sup>c</sup>different voltage polarity

Our switching fields and intercepts fall within these ranges, although our field is on the higher end (see Figure 2c and Figure S6b, *i.e.* between  $\sim 3.5$  and  $7$  V/ $\mu\text{m}$  for devices with and without a CNT, around  $T_0 = 296$  K). This is likely because our VO<sub>2</sub> films are single crystals and quite thin (higher  $R$ ) compared to others, and because our VO<sub>2</sub> has better thermal conductance (higher  $G_{\text{th}}$ ) to the crystalline TiO<sub>2</sub> substrate.

### 3. Kelvin Probe Microscopy (KPM)

During each KPM scan the device is held at a constant voltage. The current remains constant at each bias point and is shown for the VO<sub>2</sub> device without a CNT in Figure S10a and with a CNT in Figure S10b. Because  $R_s = 200$  k $\Omega$  is used, upon IMT the device voltage snaps back to  $\sim 5$  V and  $\sim 8$  V for devices with and without a CNT, respectively. The magnitude of the linear potential drop observed across the channel at each bias prior to flattening is shown for a device without a CNT in Figure S10c and with a CNT in Figure S10d. There is a slightly negative offset in the potential, which is determined by the workfunction difference between the tip and sample, as well as any error in the digital-to-analog converter.

Figures S11 and S12 show the full set of KPM scans taken with increasing  $V_s$  for the devices without and with a CNT, respectively, with labels the same as in Figure S10. These images are obtained by using a first order line flattening operation, to highlight differences in surface potential across the device width. Although this CNT had a small kink, there is no additional potential drop across it, so it is not significantly more resistive and therefore not the main cause of the heating and IMT in the VO<sub>2</sub>.

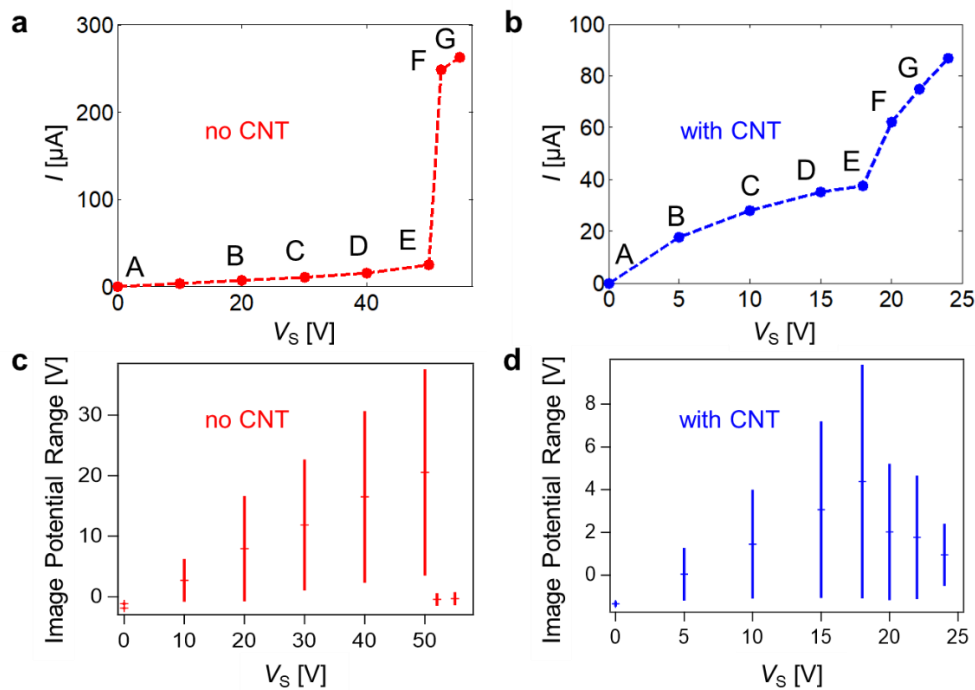


**Figure S10.** Current at each applied voltage  $V_s$  during KPM measurements of devices without (a) and with a CNT (b). Raw potential drops measured across devices without (c) and with a CNT (d) prior to flattening. The potential drops after switching because of the device voltage snapback caused by  $R_s$ .

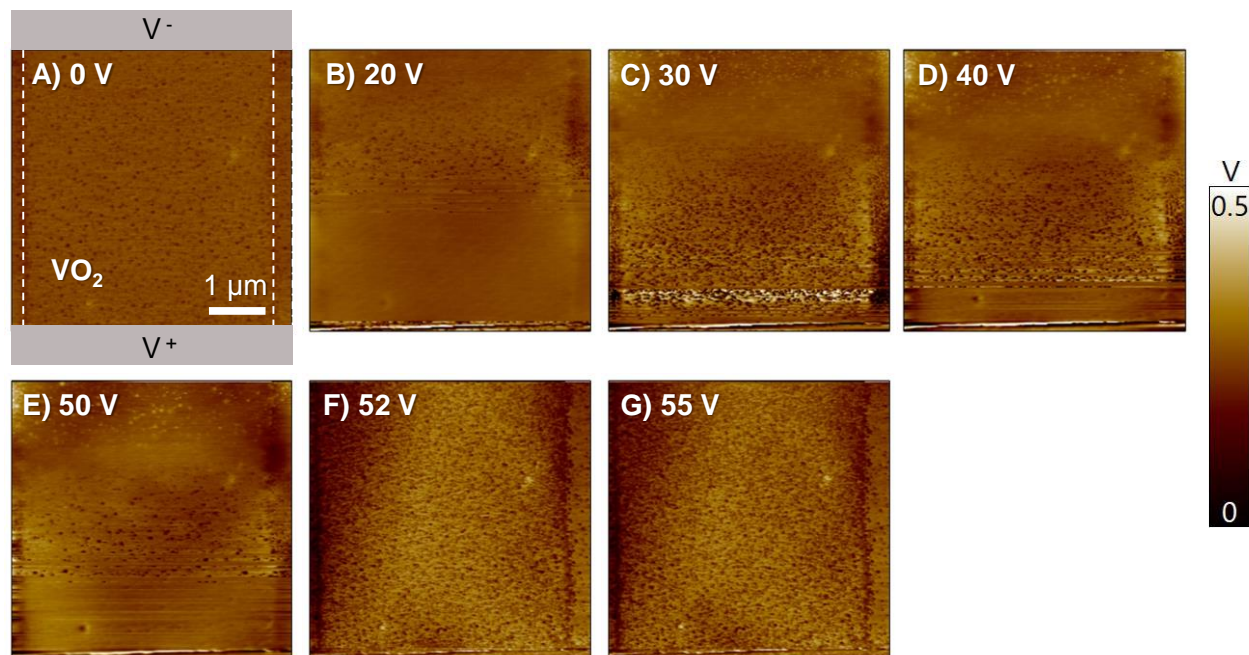


**Figure S11.** Full set of flattened KPM images of a device without a CNT. See Figure S10a for corresponding  $I$ - $V$  data. (A) is with no bias, (B) – (E) are in the insulating state, and (F) - (G) correspond to the metallic state, with applied  $V_S$  as labeled. The electrodes are just outside the images, at the top and bottom, as labelled in (A). The edges of the  $\text{VO}_2$  channel are marked in (A) with dashed lines.

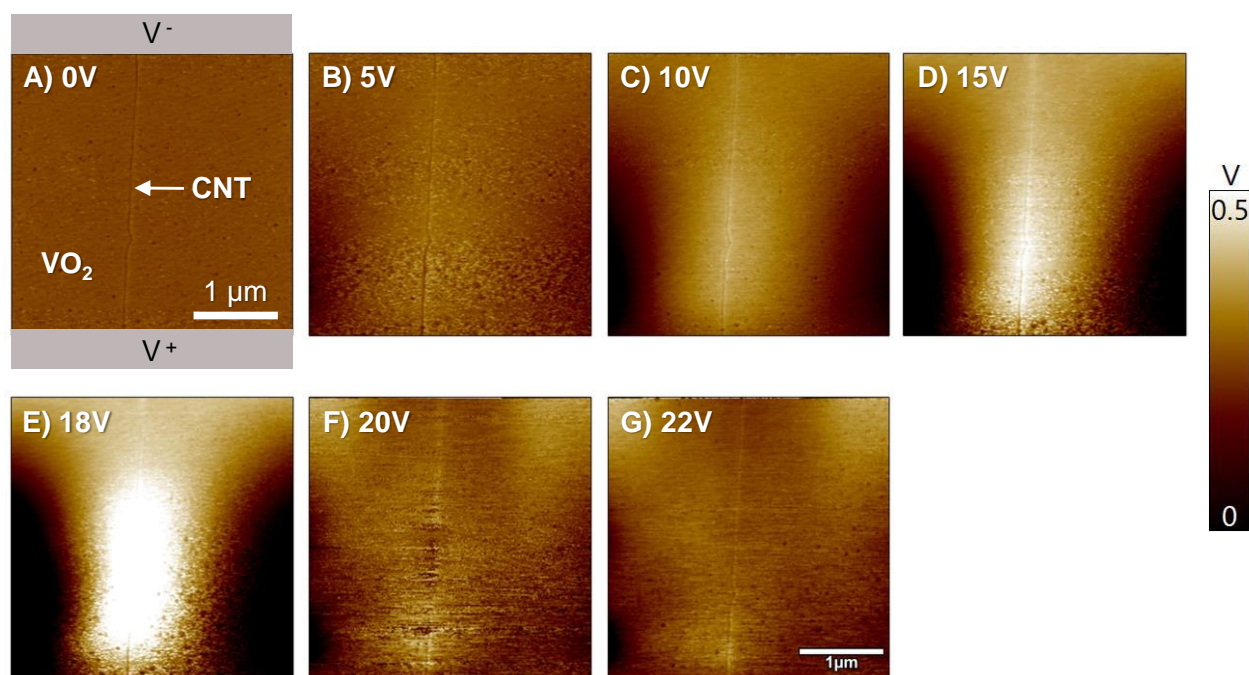


**Figure S12.** Full set of flattened KPM images of a device with a CNT. See Figure S10b for corresponding  $I$ - $V$  data. (A) is with no bias, (B) - (E) are in the insulating state, and (F) - (G) correspond to the metallic state, with applied  $V_S$  as labeled. The electrodes are just outside the images, at the top and bottom, as labelled in (A). The  $\text{VO}_2$  channel edges are just outside the images, on the left and right.

## 4. Three-Dimensional Finite Element Simulations

### 4a. Model Details

We developed a three-dimensional (3D) finite element model for our devices using COMSOL Multiphysics, which self-consistently considers electrical and thermal effects. An electrical model is used to calculate the voltage and current distribution in the device, while a thermal model determines the temperature distribution. These are coupled together *via* Joule heating, as well as by the temperature dependent resistivities of the CNT and VO<sub>2</sub>.

The model solves the following system of equations, where Eq. 1 is used to obtain the voltage and current distribution in the device while Fourier's law of heat conduction in steady state (Eq. 2) is used to obtain the local temperatures.  $k$  is the thermal conductivity, and  $\sigma$  is the electrical conductivity which is temperature dependent (and therefore spatially dependent) for the VO<sub>2</sub> and CNT. These two equations are coupled together *via*  $J \cdot E$  as a Joule heating source term, with  $J$  being the local current density and  $E$  the local electric field

$$\nabla \cdot (\sigma(x, y, z, T) \nabla V) = 0 \quad (1)$$

$$\nabla \cdot (k \nabla T) + J \cdot E = 0 \quad (2)$$

For VO<sub>2</sub>, the scaling of  $\sigma$  with temperature is based on measurements of  $R(T)$  from our films as a function of stage temperature (main text Figure 1i). A room temperature  $\sigma(296 \text{ K}) = 80 \text{ S/m}$  was extracted from this data after subtracting contact resistance, and this conductivity is then scaled with temperature according to  $R(T)/R(296 \text{ K})$ . The  $\sigma(T)$  data is imported as a table of temperature and resistance with  $\sim 1 \text{ K}$  steps. When solving it is useful to use nearest-neighbour as the interpolation type, which will round the temperature of an element to the nearest table value and use the corresponding resistance. If the default linear interpolation is used then a slight change in temperature during the IMT (the steepest part of  $\sigma(T)$ ) while solving will cause a large change in resistance between solver steps, greatly hindering convergence. Only one branch (heating or cooling) of the  $\sigma(T)$  curve is used at a time for each voltage point simulated. For generating an  $I$ - $V$  curve with hysteresis included, the heating branch was used as voltage was increased, and the cooling branch was used after switching as the voltage was swept back down. The solution for the previous voltage point was used as the initial conditions for the next voltage.

The conductivity of the CNT is based on a model developed by Pop *et al.*,<sup>3</sup> given by:

$$\sigma_{\text{CNT}}(T, V, L) = \frac{4q^2 \lambda_{\text{eff}}}{h A} \quad (3)$$

$$\text{where } \lambda_{\text{eff}} = (\lambda_{\text{AC}}^{-1} + \lambda_{\text{OP,ems}}^{-1} + \lambda_{\text{OP,abs}}^{-1} + \lambda_{\text{defect}}^{-1})^{-1} \quad (4)$$

$\lambda_{\text{eff}}$  is an effective electron mean free path (MFP) obtained using Matthiessen's rule. It combines contributions from elastic electron scattering with acoustic phonons ( $\lambda_{\text{AC}}$ ), and inelastic electron scattering by optical phonon absorption ( $\lambda_{\text{OP,abs}}$ ) and emission ( $\lambda_{\text{OP,ems}}$ ). Emission is influenced by the electric field, so this term is dependent on the applied voltage and CNT length, and all MFPs are a function of temperature. Values of  $\lambda_{\text{OP,300}} = 20 \text{ nm}$  and  $\hbar\omega_{\text{OP}} = 0.2 \text{ eV}$  are used in the model, which is described in detail in Ref. 3. An additional scattering term for defects ( $\lambda_{\text{defect}}$ ), with a mean free path of  $0.8 \mu\text{m}$ , is added to better represent  $I$ - $V$  characteristics of our imperfect CNTs. The reduction in CNT conductivity with increasing temperature results in current saturation behaviour of the CNT, described in Ref. 3 and seen in Figure S5a.

Figure S13a shows the geometry for the simulation corresponding to the device with a CNT used for SThM in main text Figure 4, and Figure S13b shows the geometry for the device simulations in main text

Figure 5. The CNT is centered in the device, so only half the device is simulated due to symmetry. The CNT is approximated as a rectangular prism 1.2 nm wide and 1.2 nm tall on top of the 5 nm thick VO<sub>2</sub>, spanning the entire length of the device and underneath the 50 nm thick Pd contacts. The simulated TiO<sub>2</sub> substrate is 2 μm thick (unlike the ~500 μm experimental TiO<sub>2</sub>), which is sufficient to capture its thermal resistance, most of which occurs at the thermal constriction near the CNT. For VO<sub>2</sub> devices without a CNT, where there is a significantly larger volume being heated, a 15 μm thick TiO<sub>2</sub> substrate needs to be simulated to accurately determine the device temperature. The device for SThM is 6 μm wide and 7 μm long, with the VO<sub>2</sub> covered by a 50 nm thick layer of poly(methyl methacrylate) (PMMA). The other simulated VO<sub>2</sub> devices with and without a CNT are 4 μm wide and 5 μm long, with no PMMA capping. For these devices, a 200 kΩ series resistor  $R_S$  is modeled as a 50 nm thick resistive layer on top of one of the contacts, with a resistivity chosen to give a total resistance of 200 kΩ. The  $R_S$  layer does not thermally interact with the device. Including the extra width of TiO<sub>2</sub> beyond the VO<sub>2</sub> width makes no significant difference to devices with a CNT (whose VO<sub>2</sub> edges are near room temperature far from the CNT heating), but a large width of TiO<sub>2</sub> is needed to fully capture the thermal profile in devices without a CNT. Material parameters are listed in Table 2.

The top of one contact is grounded, and the top of the other (or the top of  $R_S$ , if applicable) is set at a constant potential. Electrical contact resistance is simulated on internal boundaries between CNT/Pd (25 kΩ), CNT/VO<sub>2</sub> (100 kΩ) and VO<sub>2</sub>/Pd. The VO<sub>2</sub>/Pd contact resistivity is set to  $0.8 \times 10^{-3} \Omega \cdot \text{cm}^2$  (see Section 2d) at room temperature and scaled with temperature in the same way as the VO<sub>2</sub> resistivity (by using the heating branch of  $R(T)/R(296 \text{ K})$  for the forward voltage sweep and the cooling branch of  $R(T)/R(296 \text{ K})$  for the backward voltage sweep).<sup>18</sup> Other boundaries are modeled as electrically insulating.

The bottom of the TiO<sub>2</sub> is fixed at room temperature (296 K). The top of the device is assumed to be thermally insulating (adiabatic), and the sides of the device have open boundary conditions. The Pd resistivity is taken from measurements of our films, and its thermal conductivity is estimated from the Wiedemann-Franz law. Thermal boundary resistance (TBR) is simulated on all interior boundaries. These interfacial resistances cannot be ignored, since they limit the flow of heat (especially from the CNT to the VO<sub>2</sub> but also from the VO<sub>2</sub> to the TiO<sub>2</sub> substrate), impacting the local VO<sub>2</sub> temperature and therefore the switching voltage. The CNT/VO<sub>2</sub> interface is set to  $5 \times 10^{-9} \text{ m}^2 \text{K/W}$ , the TiO<sub>2</sub>/VO<sub>2</sub> interface to  $8 \times 10^{-9} \text{ m}^2 \text{K/W}$ , and all other interfaces to  $10^{-8} \text{ m}^2 \text{K/W}$ . To the authors' knowledge these have not been experimentally measured, so were adjusted within reason<sup>19</sup> to better fit the  $I$ - $V$  characteristics of the VO<sub>2</sub> device with a CNT used for SThM in main text Figure 4e.

All simulations were solved with a segregated approach, which solves each physics (temperature and voltage) sequentially, repeating until convergence is achieved. The matrix equation containing the description of the physics (Eq. 1 or 2) on each mesh element is solved using a direct approach (as opposed to iterative) with the MUMPS solver. The temperature was solved as the first step, followed by the electric potential. To help with convergence when solving across the IMT, the electric potential step was given two iterations instead of the default one (the solver will solve temperature, electric field, electric field again, temperature, *etc.* repeating until convergence). To also help simulate the IMT, the damping factors were set to 0.1 and 0.4 for the temperature and potential segregated steps respectively. The damping factor is a scaling factor reducing the size of the step taken at each iteration of the physics (rather than using the current step's solution as the next starting point, which would correspond to a damping factor of 1). If these factors are not reduced, then the solver will overshoot the solution and oscillate between insulating and completely metallic (the entire device width switched, with too much heat and current), since the problem is nonlinear.

**Table 2.** Material properties used in simulation

	$\sigma$ [S/m]	$k$ [ $\text{Wm}^{-1}\text{K}^{-1}$ ]
<b>TiO<sub>2</sub></b>	$10^{-7}$	8
<b>VO<sub>2</sub></b>	function of $T(x,y,z)$ spanning 80 to $2 \times 10^6$ (see Section 4a)	5
<b>CNT</b>	Eq. 3,4	600
<b>Pd</b>	$2.9 \times 10^6$	23
<b>PMMA</b>	$10^{-10}$	0.2

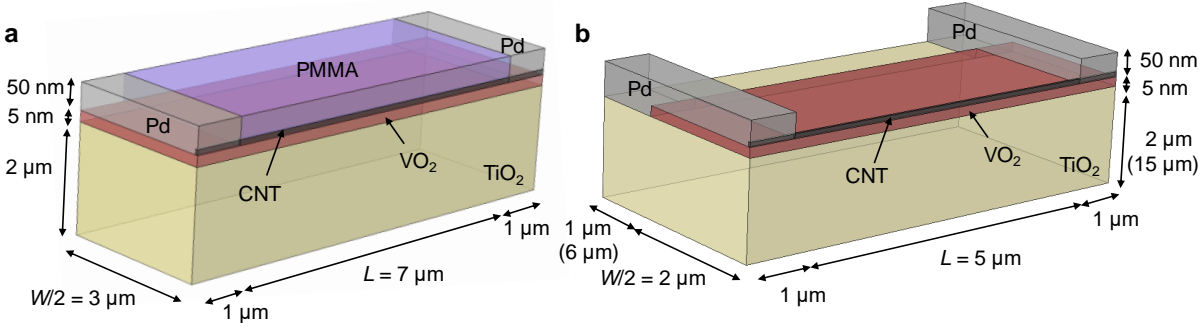


**Figure S13.** (a) Half-device structure used to simulate the experimental device used for SThM in main Figure 4. (b) Half-device structure used to simulate switching and full  $I$ - $V$  curves in main Figure 5. For the device without a CNT a larger TiO<sub>2</sub> substrate is used, with dimensions indicated in brackets.

Simulated temperatures on the surface of a VO<sub>2</sub> device without a CNT are shown just before (Figure S14a) and just after (Figure S14b) IMT, corresponding to the simulated  $I$ - $V$  curve in main text Figure 5c. Before switching there is significant bulk Joule heating, and the device requires much more power for switching than with a CNT. A  $\sim 400$  nm wide metallic “filament” is formed upon IMT in the center of the VO<sub>2</sub> device, much wider than the  $\sim 10$  nm wide “filament” in the device with a CNT. In practical devices, the filament is likely larger due to transient current overshoot, caused by parasitic capacitors discharging at the moment of switching, combined with hysteresis.

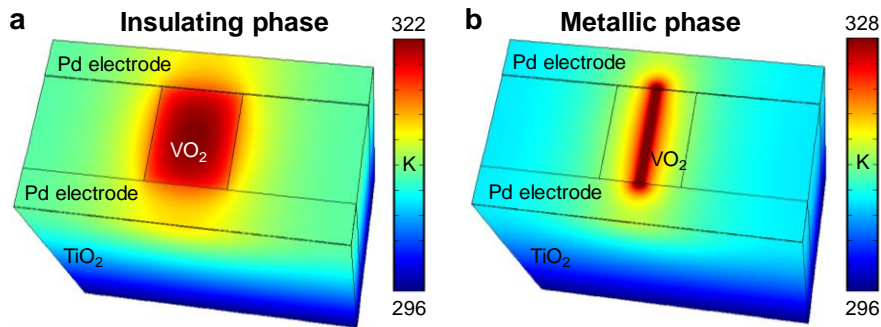


**Figure S14.** Simulated temperature on the surface of a VO<sub>2</sub> device without a CNT ( $L = 5 \mu\text{m}$ ,  $W = 4 \mu\text{m}$ ) just before (a) and just after (b) the metallic transition, with  $R_S = 200 \text{ k}\Omega$ . VO<sub>2</sub> requires a higher switching power than devices with a CNT because it relies on bulk Joule heating. After switching, a metallic region forms in the center of the device, where it is hottest, with its size determined by current overshoot and  $R_S$ . The color scalebar in (b) is cut off at  $T_{\text{IMT}} = 328 \text{ K}$  to highlight the switching region as dark red, though the temperature in the center of the metallic VO<sub>2</sub> region is higher.

#### 4b. Simulated Device Scaling

Simulated switching voltage  $V_{\text{IMT}}$ , current  $I_{\text{IMT}}$ , and power  $P_{\text{IMT}}$  of  $\text{VO}_2$  devices without a CNT are shown in Figure S15 for a variety of device lengths and widths. As device length is reduced (Figure S15a-b), both  $P_{\text{IMT}}$  and  $V_{\text{IMT}}$  decrease nearly linearly.  $I_{\text{IMT}}$  has little length dependence, with only a slight increase in very short devices. These scaling trends match well with what is seen experimentally (Figure 2c-d and Figure S3-4) and reaffirm the thermal dependence of electrical switching in  $\text{VO}_2$ .

As device width is reduced (Figure S15c-d), contact resistance increases and  $V_{\text{IMT}}$  increases steeply below  $\sim 1 \mu\text{m}$ . However,  $I_{\text{IMT}}$  also decreases, resulting in a net decrease in  $P_{\text{IMT}}$  for narrower devices. In contrast,  $\text{VO}_2$  devices with a CNT have no width dependence on switching characteristics. Given these trends, adding a CNT to an ultra-narrow  $\text{VO}_2$  device would have the benefit of maintaining a much lower, width-independent switching voltage (see Table 3 for a simulated example). However, because the CNT is more conductive than an ultra-narrow stripe of  $\text{VO}_2$ , this comes at the cost of increased insulating state current and therefore reduced on/off ratio. This could result in little improvement in overall switching power, if any. To retain access to a higher resistance state with low current, a gateable semiconducting CNT or other nonlinear heat source (*e.g.* nanowire, diode, switching material, *etc.*) could be used instead.

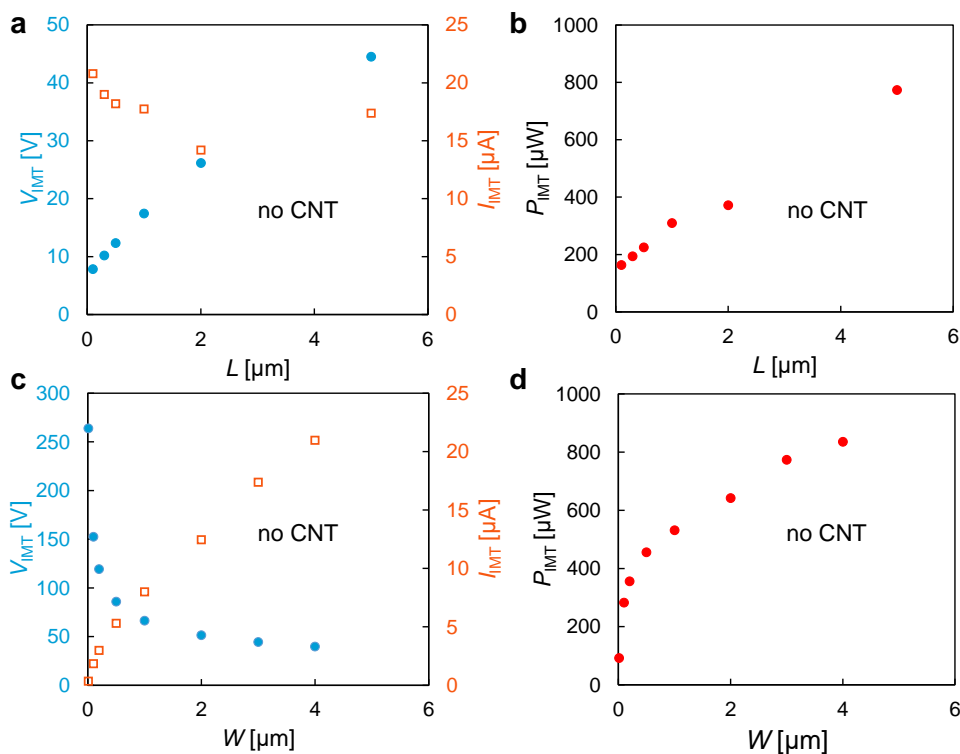


**Figure S15.** Simulated scaling trends of  $\text{VO}_2$  devices without a CNT, with thermally induced switching. (a) Switching voltage  $V_{\text{IMT}}$  (solid blue circles) decreases with device length (simulated down to 100 nm length, with  $W = 5 \mu\text{m}$ ) and switching current  $I_{\text{IMT}}$  (hollow orange squares) starts to increase slightly below  $\sim 1 \mu\text{m}$ . (b) Total device power  $P_{\text{IMT}}$  reduces linearly with length. (c) In narrow devices (simulated down to 10 nm width),  $V_{\text{IMT}}$  is much higher but  $I_{\text{IMT}}$  decreases ( $L = 5 \mu\text{m}$ ). (d) Switching power decreases as device width is reduced ( $L = 5 \mu\text{m}$ ).

**Table 3.** Simulated Switching of Narrow Devices ( $L = 5 \mu\text{m}$ ,  $W = 100 \text{ nm}$ )

	without CNT	with CNT
$V_{\text{IMT}}$ [V]	153	9
$I_{\text{IMT}}$ [ $\mu\text{A}$ ]	2	33
$P_{\text{IMT}}$ [ $\mu\text{W}$ ]	282	528

**Table 3.** Simulated switching of long, narrow  $\text{VO}_2$  devices with and without a CNT. The CNT greatly reduces the switching voltage but comes with a higher switching current and power (although the simulated CNT is more conductive than imperfect experimental CNTs). By also reducing the device length, the switching voltage and power would decrease for both types of devices.

In thermally triggered devices, there is a trade-off between low switching voltage and current because enough total power is still required to reach the transition temperature. The addition of an extra Joule heating source with an appropriate current density can shift device operation to a lower switching voltage instead of low current. Some additional control over switching voltage could be achieved by engineering the thermal environment of the device, for example, by changing the thermal boundary resistance to and the thermal conductivity of the substrate to reduce heat loss from the  $\text{VO}_2$ . If this improves heating efficiency (*e.g.* by confining heating to a small volume), then a lower switching power can be achieved.

These simulated scaling trends are estimates, assuming similar electrical and thermal transport at small length scales. In reality, there may be some differences when devices are shrunk to the nanoscale. For example, thermal and electrical conductivity of the  $\text{VO}_2$  may decrease when narrower (due to surface boundary scattering), which could affect the switching trends.

#### 4c. Models Using Other Mechanisms

We note that there are two fields at play in the devices with CNTs: the lateral field between source and drain electrodes, corresponding to  $E_{\text{IMT}}$  in Figure S6b, and the vertical field emitted by the ultra-narrow CNT into the  $\text{VO}_2$  below. A simple simulation involving the vertical field is very difficult, without knowing *e.g.* the band alignment at their interface. Therefore, we have focused on two types of simulations involving only the lateral field. In both of these, Joule heating cannot be neglected and still plays a large role, but the fundamental switching mechanism is field-driven.  $\text{VO}_2$  devices can still show switching behaviour similar to experiment, with a reduction in switching voltage seen in the devices with a CNT. Although there can be slight changes in the local field with the addition of a CNT, the reduction in switching voltage is primarily due to the heating generated by the CNT, though the increased temperature could be directly driving the transition, lowering the required field, or increasing the carrier concentration in the  $\text{VO}_2$ .

In the first model, Joule heating reduces the critical field  $E_{\text{crit}}$  required for  $\text{VO}_2$  switching. We use a linear fit to data from devices without a CNT in Figure S6b, shown in Eq. (5) in units of  $\text{V}/\mu\text{m}$ , with  $T$  being temperature in Kelvin, and  $a = -0.14 \text{ V}/\mu\text{m}/\text{K}$  and  $b = 49 \text{ V}/\mu\text{m}$  are fitting constants:

$$E_{\text{crit}} = aT + b \quad (5)$$

We note that very close to  $T_{\text{IMT}}$ , the temperature dependence of  $E_{\text{crit}}$  may not be linear, because it is expected that  $E_{\text{crit}}$  should approach zero at  $T_{\text{IMT}}$ . An alternative expression could be fitted to the data in Figure S6b:

$$E_{\text{crit}} = E_0 \sqrt{1 + T/T_{\text{IMT}}} \quad (6)$$

where  $E_0 = 25 \text{ V}/\mu\text{m}$  is a fitting constant. If switching happens considerably below  $T_{\text{IMT}}$  in the model, then the difference between Eq. (5) and (6) is found to have very little impact on switching behaviour. However,

the use of Eq. (6) ensures that the device will switch at  $T \leq T_{\text{IMT}}$ , especially in devices with a CNT where there is significant heating. The temperature dependence of the insulating state electrical conductivity of the VO<sub>2</sub> follows Eq. (7), fit with an activation energy  $E_a = 0.21$  eV and a constant  $\sigma_0 = 3 \times 10^5$  S/m to our  $R(T)$  data (main text Figure 1i).  $T$  is the temperature in Kelvin, and  $k_B = 8.617 \times 10^{-5}$  eV/K is the Boltzmann constant. The VO<sub>2</sub> conductivity increases abruptly to metallic ( $\sigma = 2 \times 10^5$  S/m) once  $E_{\text{crit}}$  is reached. The contact resistivity of the VO<sub>2</sub> to the Pd is scaled with the VO<sub>2</sub> conductivity, similar to our other simulations.

$$\sigma = \sigma_0 \exp\left(-\frac{E_a}{k_B T}\right) \quad (7)$$

In the second model, electrical conductivity in the insulating state follows a 3D Poole-Frenkel transport model<sup>20</sup> according to Eq. (8), dependent on both the electric field  $E$  and the temperature  $T$  in the device.  $\sigma_0$  and  $E_a$  were fit to experimental  $I$ - $V$  data giving  $9 \times 10^3$  A/m<sup>2</sup> and 0.22 eV respectively. A relative dielectric constant  $\epsilon_r = 38$  was used<sup>21</sup> for VO<sub>2</sub> to calculate  $\beta$  using Eq. (9). Conductivity can be converted to a carrier concentration  $n = \sigma E / (q\mu)$  using a mobility<sup>22</sup>  $\mu = 0.5$  cm<sup>2</sup>/V/s. This is compared to a critical carrier concentration  $n_c = 1.5 \times 10^{19}$  cm<sup>-3</sup> estimated from the Mott criteria for an IMT, consistent with Hall measurements of the carrier concentration at the transition point.<sup>22</sup> Once the carrier concentration exceeds  $n_c$ , the VO<sub>2</sub> becomes metallic ( $\sigma = 2 \times 10^5$  S/m). Again, the contact resistivity of the VO<sub>2</sub> to the Pd is scaled with the VO<sub>2</sub> conductivity, similar to our other simulations.

$$\sigma = \frac{\sigma_0}{E} \exp\left(-\frac{E_a}{2k_B T}\right) \left[ \left(\frac{k_B T}{\beta}\right)^2 \left(1 + \left(\frac{\beta\sqrt{E}}{2k_B T} - 1\right) \exp\left(\frac{\beta\sqrt{E}}{2k_B T}\right)\right) + \frac{E}{2} \right] \quad (8)$$

$$\beta = \sqrt{\frac{q^3}{\pi\epsilon_r\epsilon_0}} \quad (9)$$

Geometry, thermal conductivities, thermal boundary resistance, and the CNT electrical conductivity is kept the same as in our thermally-driven simulation (see Section 4a). The  $\sigma(T, E)$  data is imported as a table of local temperature, field, and resistance with  $\sim 1$  K steps. When solving it is best to avoid using nearest-neighbour as the interpolation type, which will produce artifacts in the local field. Because of the stronger coupling of the field to conductivity, the problem becomes increasingly nonlinear. This makes it very challenging to reach convergence in the metallic state, so we have only simulated up to the IMT.

In the temperature-dependent electric field model using Eq. (5) to (7), the switching voltage of a device without a CNT is  $\sim 34$  V, considerably lower than experiments and other models shown in Figure S16. Switching occurs at a much lower temperature ( $\sim 315$  K) than  $T_{\text{IMT}}$ . In devices with a CNT, the switching voltage is reduced to  $\sim 11$  V and the VO<sub>2</sub> temperature reaches  $\sim T_{\text{IMT}}$  underneath the CNT. Increasing thermal properties within reason for devices without a CNT in order to reduce the VO<sub>2</sub> temperature ( $k_{\text{TiO}_2} = 15$  Wm<sup>-1</sup>K<sup>-1</sup>,  $k_{\text{VO}_2} = 7$  Wm<sup>-1</sup>K<sup>-1</sup>, and a TiO<sub>2</sub>/VO<sub>2</sub> interface TBR =  $5 \times 10^{-9}$  m<sup>2</sup>K/W) only slightly raises the switching voltage by  $\sim 2$  V and *cannot* reproduce the experimental switching voltage. However, it is likely that  $E_{\text{crit}}$  at a given temperature is higher than that given by fits to Figure S6b, since the local device temperature is higher than the ambient temperature. Increasing the required field at a given temperature by setting  $b = 54$  V/ $\mu\text{m}$  in Eq. (5) or  $E_0 = 40$  V/ $\mu\text{m}$  in Eq. (6), and using the original thermal properties in Table 2, fits experimental data for devices without a CNT much more closely, shown as “ $E_c$  sim” in Figure S16. When Eq. (6) with  $E_0 = 40$  V/ $\mu\text{m}$  is used to simulate devices with a CNT, the switching voltage remains  $\sim 10$  V even with the higher required field, because switching is set more by the VO<sub>2</sub> reaching  $T \sim T_{\text{IMT}}$  (where  $E_{\text{crit}} \sim 0$ ) than by changes in the local field induced by the CNT.

Both field-based models can then produce electrical switching behaviour similar to experiment, shown in Figure S16 for devices with and without a CNT. Thus, we cannot rule out a thermally-assisted transition based on reaching a critical field or carrier concentration, rather than just a critical temperature. All models show a similar reduction in switching voltage for devices with a CNT when compared to VO<sub>2</sub> devices without a CNT, due to the heating of the VO<sub>2</sub> by the CNT.

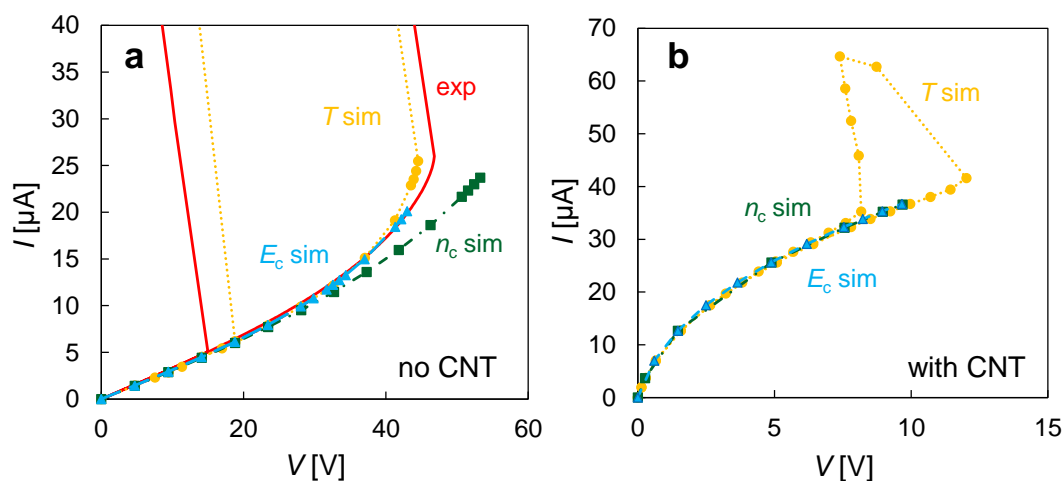


**Figure S16.** Simulated voltage-controlled  $I$ - $V$  curves for  $\text{VO}_2$  devices without (a) and with (b) a CNT ( $L = 5 \mu\text{m}$ ,  $W = 4 \mu\text{m}$  for the  $\text{VO}_2$ ). Several models are used: a model where the IMT depends only on temperature (labelled “ $T$  sim”, orange dots), a model where IMT is triggered by a temperature-dependent critical electric field (labelled “ $E_c$  sim”, blue dashes and triangles), and a model where IMT is triggered by a critical carrier concentration dependent on temperature and electric field (labelled “ $n_c$  sim”, dark green dot-dashes and squares). In models with a field dependence, the last data point shown is just before IMT.

### 5. Supplementary Video

Video S1 (uploaded separately) shows the evolution of surface temperature of the simulated device with a CNT (main Figure 5a), as the voltage is swept up and then down on the  $I$ - $V$  curve (main Figure 5b).

### 6. Supplementary References

1. Jeong, J.; Aetukuri, N.; Graf, T.; Schladt, T. D.; Samant, M. G.; Parkin, S. S., Suppression of Metal-Insulator Transition in  $\text{VO}_2$  by Electric Field-Induced Oxygen Vacancy Formation. *Science* **2013**, 339, 1402-1405.
2. Patil, N.; Lin, A.; Myers, E. R.; Kounghmin, R.; Badmaev, A.; Chongwu, Z.; Wong, H. S. P.; Mitra, S., Wafer-Scale Growth and Transfer of Aligned Single-Walled Carbon Nanotubes. *IEEE Trans. Nanotechnol.* **2009**, 8, 498-504.
3. Pop, E.; Mann, D. A.; Goodson, K. E.; Dai, H., Electrical and Thermal Transport in Metallic Single-Wall Carbon Nanotubes on Insulating Substrates. *J. Appl. Phys.* **2007**, 101, 093710.
4. Yoon, J.; Lee, G.; Park, C.; Mun, B. S.; Ju, H., Investigation of Length-Dependent Characteristics of the Voltage-Induced Metal Insulator Transition in  $\text{VO}_2$  Film Devices. *Appl. Phys. Lett.* **2014**, 105, 083503.
5. Wan, H. J.; Zhou, P.; Ye, L.; Lin, Y. Y.; Tang, T. A.; Wu, H. M.; Chi, M. H., *In Situ* Observation of Compliance-Current Overshoot and Its Effect on Resistive Switching. *IEEE Electron Device Lett.* **2010**, 31, 246-248.
6. Yu, S.; Guan, X.; Wong, H.-S. P., Understanding Metal Oxide RRAM Current Overshoot and Reliability Using Kinetic Monte Carlo Simulation. *IEEE Int. Electron Devices Meet.* **2012**.
7. Aetukuri, N. P. B. The Control of Metal-Insulator Transition in Vanadium Dioxide. Ph.D. Thesis, Stanford University, 2013, <https://searchworks.stanford.edu/view/10163818>.

8. Li, D.; Sharma, A. A.; Gala, D. K.; Shukla, N.; Paik, H.; Datta, S.; Schlom, D. G.; Bain, J. A.; Skowronski, M., Joule Heating-Induced Metal-Insulator Transition in Epitaxial VO<sub>2</sub>/TiO<sub>2</sub> Devices. *ACS Appl. Mater. Interfaces* **2016**, *8*, 12908-12914.
9. Vitale, W. A.; Tamagnone, M.; Moldovan, C. F.; Emond, N.; Casu, E. A.; Petit, L.; Le Drogoff, B.; Chaker, M.; Mosig, J. R.; Ionescu, A. M., Field-Enhanced Design of Steep-Slope VO<sub>2</sub> Switches for Low Actuation Voltage. *Proc. Eur. Solid-State Device Res. Conf.* **2016**.
10. Joushaghani, A.; Jeong, J.; Paradis, S.; Alain, D.; Stewart Aitchison, J.; Poon, J. K. S., Voltage-Controlled Switching and Thermal Effects in VO<sub>2</sub> Nano-Gap Junctions. *Appl. Phys. Lett.* **2014**, *104*, 221904.
11. Vitale, W. A.; Moldovan, C. F.; Tamagnone, M.; Paone, A.; Schuler, A.; Ionescu, A. M., Steep-Slope Metal-Insulator-Transition VO<sub>2</sub> Switches with Temperature-Stable High I<sub>ON</sub>. *IEEE Electron Device Lett.* **2015**, *36*, 972-973.
12. Madan, H.; Jerry, M.; Pogrebnyakov, A.; Mayer, T.; Datta, S., Quantitative Mapping of Phase Coexistence in Mott-Peierls Insulator during Electronic and Thermally Driven Phase Transition. *ACS Nano* **2015**, *9*, 2009-2017.
13. Radu, I. P.; Govoreanu, B.; Mertens, S.; Shi, X.; Cantoro, M.; Schaekers, M.; Jurczak, M.; De Gendt, S.; Stesmans, A.; Kittl, J. A.; Heyns, M.; Martens, K., Switching Mechanism in Two-Terminal Vanadium Dioxide Devices. *Nanotechnology* **2015**, *26*, 165202.
14. Kim, H.-T.; Chae, B.-G.; Youn, D.-H.; Kim, G.; Kang, K.-Y.; Lee, S.-J.; Kim, K.; Lim, Y.-S., Raman Study of Electric-Field-Induced First-Order Metal-Insulator Transition in VO<sub>2</sub>-Based Devices. *Appl. Phys. Lett.* **2005**, *86*, 242101.
15. Kim, B.-J.; Lee, Y. W.; Choi, S.; Yun, S. J.; Kim, H.-T., VO<sub>2</sub> Thin-Film Varistor Based on Metal-Insulator Transition. *IEEE Electron Device Lett.* **2010**, *31*, 14-16.
16. Zimmers, A.; Aigouy, L.; Mortier, M.; Sharoni, A.; Wang, S.; West, K. G.; Ramirez, J. G.; Schuller, I. K., Role of Thermal Heating on the Voltage Induced Insulator-Metal Transition in VO<sub>2</sub>. *Phys. Rev. Lett.* **2013**, *110*, 056601.
17. Kim, H.-T.; Kim, B.-J.; Choi, S.; Chae, B.-G.; Lee, Y. W.; Driscoll, T.; Qazilbash, M. M.; Basov, D. N., Electrical Oscillations Induced by the Metal-Insulator Transition in VO<sub>2</sub>. *J. Appl. Phys.* **2010**, *107*, 023702.
18. Martens, K.; Radu, I. P.; Mertens, S.; Shi, X.; Nyns, L.; Cosemans, S.; Favia, P.; Bender, H.; Conard, T.; Schaekers, M.; De Gendt, S.; Afanas'ev, V.; Kittl, J. A.; Heyns, M.; Jurczak, M., The VO<sub>2</sub> Interface, the Metal-Insulator Transition Tunnel Junction, and the Metal-Insulator Transition Switch On-Off Resistance. *J. Appl. Phys.* **2012**, *112*, 124501.
19. Pop, E., Energy Dissipation and Transport in Nanoscale Devices. *Nano Res.* **2010**, *3*, 147-169.
20. Gibson, G. A.; Musunuru, S.; Zhang, J.; Vandenberghe, K.; Lee, J.; Hsieh, C.-C.; Jackson, W.; Jeon, Y.; Henze, D.; Li, Z.; Williams, R. S., An Accurate Locally Active Memristor Model for S-Type Negative Differential Resistance in NbO<sub>x</sub>. *Appl. Phys. Lett.* **2016**, *108*, 023505.
21. Yang, Z.; Ko, C.; Balakrishnan, V.; Gopalakrishnan, G.; Ramanathan, S., Dielectric and Carrier Transport Properties of Vanadium Dioxide Thin Films across the Phase Transition Utilizing Gated Capacitor Devices. *Phys. Rev. B* **2010**, *82*, 205101.
22. Ruzmetov, D.; Heiman, D.; Claflin, B. B.; Narayanamurti, V.; Ramanathan, S., Hall Carrier Density and Magnetoresistance Measurements in Thin-Film Vanadium Dioxide across the Metal-Insulator Transition. *Phys. Rev. B* **2009**, *79*, 153107.